Systematic Studies of the Deconvolution of Gamma-Ray Images

Master's Thesis in Physics

Presented by
Carolin Wunderlich
January 11, 2019

Erlangen Centre for Astroparticle Physics
Friedrich-Alexander-Universität Erlangen-Nürnberg

Supervisor: PD Dr. Ira Richard-Jung

Second referee: Prof. Dr. Stefan Funk

Contents

1 Introduction

Most of the radiation which spreads through the universe and enters our atmosphere is thermal radiation. It is generated by hot objects like stars. However, a certain amount of this radiation has no thermal origin. The best-known example for non-thermal radiation are galactic cosmic rays and extragalactic cosmic rays. In contrast to the radiation emitted by stars, their power-law spectrum is not correlated to the temperature. Furthermore, the energies of extragalactic cosmic rays up to 10^{20} eV are that high that their origin is not conceivable by any known thermal emission mechanism [1].
The exploration of cosmic rays began in the year 1912, when the Austrian physicist Victor Hess discovered cosmic rays in his famous balloon experiments. By using a balloon he measured an increasing ionisation from an altitude of 1 km. He concluded that high-energy cosmic particles entered the atmosphere, namely cosmic rays [2]. For his discovery, he was awarded the Nobel Prize in Physics in the year 1936. Since then, cosmic rays and the details of their origin have been of particular interest in the field of research. Nowadays it is supposed that cosmic particle accelerators, for example rotating neutron stars, pulsars, active galactic nuclei and shock wave fronts of supernova explosions, are the origin of cosmic rays. In these accelerators charged particles such as protons (hydrogen nuclei), α-particles (helium nuclei), nuclei from more massive elements and electrons are accelerated to high energies until they leave the accelerator and start to spread throughout the universe [1, 3].
The research of cosmic ray sources is challenging since charged particles are deflected by galactic and intergalactic magnetic fields. In contrast, it is possible to observe gamma-rays, which are generated as secondary particles of cosmic rays during their interaction with the ambient medium. Gamma-rays have the advantage that they can be traced directly back to their origin. By observing cosmic gamma-rays, it is therefore possible to localise the above-named cosmic accelerators [1].

Gamma-rays and cosmic rays can be measured in different ways. One possibility are space observatory satellites like the Fermi Gamma-ray Space Telescope. However, such satellites only have a limited detector size due to cost and constructional reasons. Because of the small flux of gamma-rays for higher energies, it is not possible to measure them with space observatory satellites. In order to determine very high energy (VHE) gamma-rays for energies between 10^{11} to 10^{14} eV, ground-based telescopes via the Imaging Atmospheric Cherenkov Technique are used (cf. Chapter 3). These telescopes measure the Cherenkov light of air showers. Those are generated when cosmic rays or gamma-rays enter the atmosphere. One experiment which uses the Imaging Atmospheric Cherenkov Technique is the High Energy Stereoscopic System (H.E.S.S.). It was named after Victor Hess. Further information about H.E.S.S. will be given in Chapter 3. In Figure 1.1, one of the small telescopes of H.E.S.S. is shown together with galactic VHE gamma-ray sources along the galactic plane.

Supernova remnants (SNR) are prime candidates as sources of galactic VHE gamma-rays and will be introduced in Chapter 2. So far, the detailed nature of the generation of gamma-rays in the acceleration process within SNRs has not been clearly understood. Either mainly leptonic or mainly hadronic particles are accelerated in the SNRs. Thus, a leptonic or a hadronic scenario are a possible origin of gamma-rays. To investigate this topic further, it is necessary to study the morphology of a supernova remnant in more detail. Thereby, the resolution of the gamma-ray data plays a key role. The resolution can be improved by applying deconvolution algorithms to the data. Yet it is important to understand, in which way spacial deconvolution affects the data and how the development of deconvolution depends on the characteristics of the source like its morphology or brightness.
In order to study deconvolution algorithms in the field of gamma-ray astronomy, simulations of supernova remnants with different morphologies are a reasonable starting point. In the context of this Master's thesis, two different deconvolution algorithms are introduced in Chapter 4: the Richardson-Lucy algorithm and the Maximum-Entropy algorithm. This is followed by the explanation of the simulation of gamma-ray images in general and for sources with different morphologies (cf. Chapter 5). Moreover, the development of deconvolution depending on the iteration steps of the algorithm (in particular for the Richardson-Lucy algorithm) and different aspects of the source are discussed. The results of this study are presented in Chapter 6 and in Chapter 7. Finally, the well-known supernova remnant RX J1713.7-3946 is examined. This thesis concludes with a demonstration of an application of deconvolution algorithms in the case of a correlation study between deconvoluted gamma-ray data and X-ray data of RX J1713.7-3946 (cf. Chapter 8). It is intended to illustrate, how deconvolution algorithms help to improve the investigation of the morphology of SNRs.

Figure 1.1: Photo montage of the night sky over Namibia with the H.E.S.S. map of the galactic plane survey. The telescope in the foreground is one of the small H.E.S.S. telescopes. The red spots in the background are VHE gamma-ray sources observed by H.E.S.S. [4].

2 Supernova Remnants

This chapter is an introduction to supernova remnants. The current knowledge of their evolution and morphology is presented. Moreover, their role as galactic VHE gamma-ray accelerators and in particular the two radiation scenarios which contribute to the production of VHE gamma radiation are discussed.

2.1 Evolution and Morphology

During the explosion of a supernova, high energetic gas is ejected into the interstellar medium (ISM). In the following, the evolution of the supernova remnant is explained. In total four phases are distinguished:

Phase I: Free Expansion Phase

In the free expansion phase, a shock front is formed by the interaction between the ISM and the ejected gas. Thereby, a shell structure is formed. During the process, the gas from the SNR is slowed down [5]. SNRs in the free expansion phase can be identified by the lack of hydrogen lines in their spectra. The radius R of the SNR is proportional to the age t of the SNR.

$$R \propto t \tag{2.1}$$

The phase ends when the order of swept-up-mass of the ISM is comparable to the amount of ejected mass [6].

Phase II: Sedov-Taylor Phase

In the Sedov-Taylor Phase, the swept-up matter dominates the supernova remnant. The energy is conserved because radiative losses are negligible. The phase can be described by

$$R^3 v^2 = \text{constant.} \tag{2.2}$$

R denotes the radius of the remnant and v the velocity of the shock. From Equation 2.2 follows that the velocity of the shock decreases with increasing radius. Thus, the kinetic and thermal energies are separately conserved [5]. The Sedov-Taylor phase ends when the energy loss due to radiative cooling is no longer negligible [6].

Phase III: Snowplough Phase

In the Snowplough Phase, the matter behind the shock cools quickly [5]. The cooling losses take away most of the shock energy and the shell moves at a constant radial momentum [6].

Phase IV: Dispersal Phase

The interstellar gas which surrounds the SNR moves randomly. In the Dispersal Phase, the velocity of the shell becomes comparable to the sound velocity of the ISM. The SNR is dispersed by these random motions. Finally it loses its identity and merges into the ISM [5, 6].

Morphology

On the basis of radio observations, it is understood that there exist at least three different types of SNR morphologies [7]. The three types of morphology are:

- Shell type remnants:
  The vast majority of observed SNRs show a shell type morphology. They have the appearance of a ring-shaped structure with nearly no central emission. The evolution of a SNR described above, refers to a shell-like morphology [7].

- Crab-like remnants:
  These SNRs are centrally-filled, containing a pulsar additional to the shock wave front. An example of this morphology is the Crab nebula [7].

- Composite remnants:
  There have also been observed SNRs with a “hybrid” morphology. They have a shell structure, but the shell is further surrounded by a centrally condensed nebula. It looks like a hybrid of the first two morphologies, depending on the waveband which is observed [7].

2.2 Diffusive Shock Acceleration

In SNRs, cosmic rays are accelerated through a diffusive shock acceleration mechanism. This acceleration mechanism is described by the first-order Fermi acceleration in the presence of strong shock waves. Historically seen the second-order Fermi acceleration mechanism was proposed before.

2.2.1 The Second-Order Fermi-mechanism

The idea of the second-order mechanism is that particles can be accelerated to high energies by colliding with clouds in the ISM. In the original description by Fermi, charged particles are reflected from randomly moving "magnetic mirrors" and gain energy stochastically from these reflections [8, 9].

The mirrors are presumed as infinitely massive. Hence, their velocity v does not change during the collision. With the angle θ between the initial direction of the particle and the surface of the mirror and γ_L the Lorentz factor, the energy E' of a particle with initial energy E after the collision in the centre of momentum frame is

$$E' = \gamma_L (E + vp\cos\theta). \tag{2.3}$$

The relativistic momentum p in x-direction is

$$p'_x = \gamma_L \left(p\cos\theta + \frac{vE}{c^2} \right). \tag{2.4}$$

The energy of the particle is conserved. Its momentum in x-direction is reversed after the collision. E'' denotes the energy of the particle after the collision in the observer's frame.

$$E'' = \gamma_L (E' + vp'_x) \tag{2.5}$$

Using Equation 2.4 and 2.5 and $p_x/E = v\cos\theta/c^2$ with v_p the velocity of the particle, we get

$$E'' = \gamma_L E \left[1 + \frac{2vv_\mathrm{p} cos\theta}{c^2} + \left(\frac{v}{c} \right)^2 \right]. \tag{2.6}$$

After applying the Taylor expansion on Equation 2.6 and calculating $\Delta E = E'' - E$, the result is integrated over all angles in the range 0 to π. As a result, one gets the average energy increase of a particle per collision:

$$\left\langle \frac{\Delta E}{E} \right\rangle = \frac{8}{3} \left(\frac{v}{c} \right)^2. \tag{2.7}$$

However, there are some problems with this assumption that collisions of interstellar clouds are the main acceleration source of charged particles. One problem is that random velocities of clouds in the interstellar medium are quite small compared to the speed of light ($V/c \leq 10^{-4}$). Another problem is that the free path for the scattering of cosmic rays in the ISM is very long (in the order of 0.1 pc). This corresponds to only few collisions per year. The energy gain process of the particle would be really slow. However, the describe acceleration process fits better to the shells of young SNRs since their velocities are much higher and more structure is present [8, 9].

2.2.2 The First-Order Fermi-mechanism

In the first-order Fermi acceleration mechanism, particles are accelerated by propagating through strong shock wave fronts of supernova explosions. It is assumed that high energy particles are in front of and behind the shock front. The particles' velocity is close to the speed of light. As the gyroradius of such particles is quite small compared to the shock front, they hardly notice the propagation throughout the shock front. The gyroradius of a charged particle is the radius of its circular movement in a magnetic field. By performing a Lorentz transformation the energy of a particle increases by propagating through the shock:

$$E' = \gamma_V (E + v p_x). \tag{2.8}$$

The shock is assumed to be non-relativistic ($\gamma_L = 1$), but the particles are relativistic. Therefore, we get

$$\Delta E = pv \cos\theta. \tag{2.9}$$

For every propagation through the shock front, a particle gains a energy of

$$\left\langle \frac{\Delta E}{E} \right\rangle = \frac{2}{3} \left(\frac{v}{c} \right)^2 . \tag{2.10}$$

and for a roundtrip:

$$\left\langle \frac{\Delta E}{E} \right\rangle = \frac{4}{3} \left(\frac{v}{c} \right)^2 . \tag{2.11}$$

2.3 Gamma Radiation

In the previous chapter an acceleration mechanism in SNRs was introduced. In the following, different processes in which VHE gamma-rays are produced by high energetic protons or electrons are discussed. VHE gamma-rays originate either from accelerated leptons or hadrons. The question is which one is mainly responsible for the production of VHE gamma-rays in SNR.

2.3.1 Hadronic Gamma-Ray Production

If protons are accelerated in a cosmic source as described in Section 2.2, they can interact with other protons or nuclei and produce charged and neutral pions [10]. A possible process is

$$p + \text{nucleus} \;\rightarrow\; p' + \text{nucleus}' + \pi^+ + \pi^- + \pi^0. \tag{2.12}$$

Charged pions decay into muons and neutrinos, whereas neutral pions decay with a short live time of only $\tau = 8.4 \times 10^{-17}$ s into two γ quants:

$$\pi^0 \;\rightarrow\; \gamma + \gamma. \tag{2.13}$$

2.3.2 Leptonic Gamma-Ray Production

There are three main processes through which an electron or a positron can lose its energy in the ISM: Synchrotron radiation, bremsstrahlung and inverse compton scattering. Hereinafter these three processes are presented.

Synchrotron Radiation

A particle with a charge ze, which moves with a velocity $\vec{v}$ in a magnetic field $\vec{B}$, is accelerated and deflected on a spiral path by the Lorentz force $\vec{F}$:

$$\vec{F} = ze(\vec{v} \times \vec{B}). \tag{2.14}$$

Because of the acceleration, the particle emits electromagnetic radiation, the so-called synchroton radiation (cf. Equation 2.15). It is the correspondent to bremsstrahlung in electric fields.

$$-\left(\frac{\mathrm{d}E}{\mathrm{d}t}\right)_S = \frac{4}{3}\sigma_T c u_{mag}\left(\frac{v^2}{c^2}\right)\gamma_L^2 \tag{2.15}$$

u_{mag} denotes the energy density of the magnetic filed and σ_T the so called Thomson cross-section, which denotes the total cross-section for the scattering of electromagnetic waves with stationary free electrons. Synchrotron radiation has a main contribution to the non-thermal X-ray and gamma-continuum emissions. The term “non-thermal” means that the continuum radiation originates from particles with a non-Maxwellian energy spectrum [9].

Bremsstrahlung

If a charged particle passes the electric field of another charged particle, for example an atomic nucleus or an electron, it is deflected and decelerated. As a result it emits bremsstrahlung. By defining a radiation length X_0 over which the electron has only $1/e$ of its initial energy, the energy loss per distance is

$$-\left(\frac{\mathrm{d}E}{\mathrm{d}x}\right)_B = \frac{E}{X_0}. \tag{2.16}$$

The energy loss per time is than described by

$$-\left(\frac{\mathrm{d}E}{\mathrm{d}t}\right)_B = \frac{Ec}{X_0}. \tag{2.17}$$

For high energy electrons bremsstrahlung is the main energy loss mechanism [9].

Inverse Compton Scattering

In inverse Compton scattering (IC) relativistic electrons scatter with low energy photons. Through the scattering, the photons gain kinetic energy of the electrons while in the Compton scattering the photons lose energy to the electrons, which is described by Equation 2.18. Through this process high energetic photons can be produced. In the following the case of non-relativistic electrons ($\gamma_L << 1$) is considered. Thus, the Thomson scattering cross-section σ_T can be used to describe the probability of scattering.

$$-\left(\frac{\mathrm{d}E}{\mathrm{d}t}\right)_{IC} = \frac{4}{3}\sigma_T c u_{rad}\left(\frac{v^2}{c^2}\right)\gamma^2, \tag{2.18}$$

u_{rad} denotes the energy density of radiation. There is a clear similarity to Equation 2.15 of the synchrotron radiation. The reason for that is the dependency of the energy loss rate on the acceleration through the electric field whereas the origin of the electric field does not matter. For the synchrotron radiation the electric field is the $(\vec{v} \times \vec{B})$-field and for the inverse Compton scattering the electric field is the sum of electric fields of the electric waves which incident upon the electron [9].

3 Ground-based Gamma-Ray Telescopes

In the previous chapter the generation of gamma radiation and supernova remnants as a source of gamma radiation were introduced. It is possible to measure this radiation outside the atmosphere with space observatories, for example with the Fermi satellite. However, for high energies the flux of gamma radiation is quite low. This leads to an upper limit of the detectable energy range because of the relatively small size of the detector surface of Fermi. This in turn caused by high cost factors for satellites.

Another possibility to detect gamma radiation is the so-called Imaging Atmospheric Cherenkov Technique (IACT) which uses ground-based telescopes. In this case the earth's atmosphere is the detector material. The telescopes measure Cherenkov radiation, emitted by secondary particles of air showers, which are caused by highly energetic particles. Thus, this technique enables to measure gamma radiation at higher energies compared to space observatories.

In this chapter, the development of particle showers which are initiated by gamma-rays and cosmic rays entering the atmosphere are explained. Afterwards, the emission of Cherenkov radiation by superluminal charged particles is discussed. Finally, further information about telescopes using the IACT and in particular the High Energy Stereoscopic System (H.E.S.S.) is given.

3.1 Air Showers

When a highly energetic particle enters the atmosphere, a particle shower is generated. These showers can have either electrons, positrons or photons as their origin or hadronic particles like protons or nuclei. In the case of electrons, positrons and photons the shower is termed as electromagnetic shower. Air showers initiated by hadronic particles are called hadronic showers.

3.1.1 Electromagnetic Shower

When an electron, positron or photon enters the atmosphere, it interacts either via pair production or bremsstrahlung. A gamma-ray, which is equal to a highly energetic photon, generates an electron-positron pair due to pair production with atmospheric nuclei. The photon transfers almost its whole energy to the the electron and the positron, only a small part of the photon energy is transformed to the recoil energy of the nucleus [11]. Electrons and positrons themselves can also interact with the atmosphere via bremsstrahlung. Withal

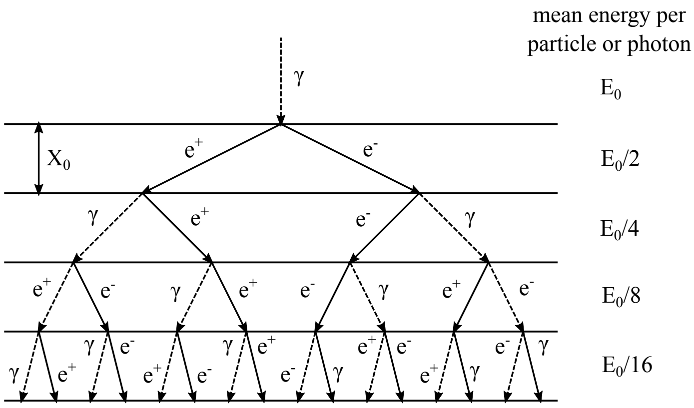

Figure 3.1: The Heitler model of an electromagnetic shower: it is assumed that the particles generated in pair production or bremsstrahlung share the energy E_0 of the primary photon equally and that the radiation length X_0 is fixed. Adapted [12, 13].

an electron or positron is scattered in the Coulomb field of a nucleus and emits at least one photon. The processes of pair production and of bremsstrahlung repeat until the energy of the secondary photons is too small for further pair production. The emergence of a cascade of secondary electrons, positrons and photons caused by a gamma-ray is called an electromagnetic shower.

In Figure 3.1 the simplified model of an electromagnetic shower by Erwin Heitler is shown. In the Heitler model electrons, positrons and photons undergo either one-photon bremsstrahlung or pair production after a fixed radiation length of X_0. Thus the number of particles in the shower has doubled and the energy per particle has halved. After n repetitions the maximal number of particles $N_{\max}$ in the shower is 2^n.

Hence, $N_{\max}$ is proportional to the energy E_0 of the primary photon and the maximal depth of the shower $X_{0,\max}$ is logarithmically proportional to E_0, which is described by Equation 3.1 [9, 12].

$$X_{0,\max} = X_0 \ln N_{\max} \tag{3.1}$$

To simplify, several assumptions were made. In reality, the radiation length X_0 is not fixed, but differs for pair production and bremsstrahlung. Furthermore the energy is not equally shared in the process of bremsstrahlung, neither is always only one photon produced. Nevertheless, the model can correctly describe the most important features of electromagnetic showers, as the proportional relation between the size of the shower and E_0 or the logarithmic proportional increase of the depth of shower with E_0 [12].

3.1.2 Hadronic Shower

Besides electrons, positrons and photons, hadronic particles like cosmic protons or nuclei enter the atmosphere. They interact with nuclei of the earth's atmosphere and give rise to a large

number of secondary particles. The secondary particles interact with atmospheric particles as well, generating more secondary particles, which form a nucleonic cascade. These cascades are the hadronic equivalent to electromagnetic showers. The cosmic background in gamma-ray observations is composed by cosmic rays.
The majority of secondary particles are pions. Charged pions interact with nuclei in the atmosphere and generate secondary pions. This process repeats until the energy of the charged pions drops below a critical value of 1 GeV, the amount of energy which is needed for pion production. At this point, the charged pions begin to decay into muons (cf. Equation 3.2). Thereby, a neutrino or an antineutrino is emitted [9, 12].

$$\pi^+ \rightarrow \mu^+ + \nu_\mu \pi^- \rightarrow \mu^- + \bar{\nu}_\mu \tag{3.2}$$

Low energy muons decay further into a positron or electron, as well as an electron and muon neutrino or antineutrino (cf. Equation 3.3).

$$\mu^+ \rightarrow e^+ + \nu_e + \bar{\nu}_\mu \mu^- \rightarrow e^- + \bar{\nu}_e + \nu_\mu \tag{3.3}$$

Neutral pions on the other hand decay immediately into two photons as already stated in Chapter 2.3.1. The photons can initiate electromagnetic showers themselves.

$$\pi^0 \rightarrow \gamma + \gamma \tag{3.4}$$

Other particles which are generated in the cascade besides pions are strange particles and antinucleons. Hence, hadronic showers have three different components of secondary particles, which are shown in Figure 3.2 [14]:

- The soft component is the electromagnetic part of the shower, consisting of electrons, positrons and photons. Since the energy of the primary particle in this part of the hadronic cascade is quite fast distributed, it is called soft component.
- The hadronic component consists of various hadronic particles. The vast amount of them are pions.
- The hard component are muons and neutrions, which are generated in the pion decay. Muons have a quite low interaction probability. Thus, this part of the hadronic shower is called hard component.

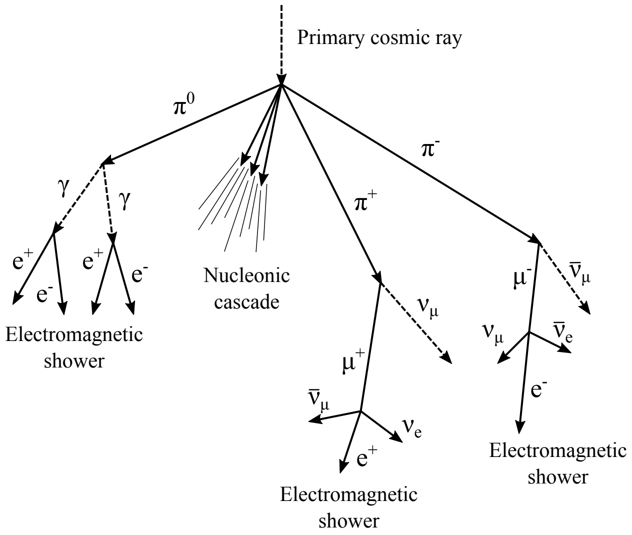

Figure 3.2: A schematic sketch of the development of a hadronic shower, which consists of nucleonic cascades and electromagnetic showers. The composition of a hadronic shower can furthermore be divided in three components: the electromagnetic component, also referred to as soft component, the hadronic component, consisting mainly of pions, and the hard component, comprised of muons and neutrinos. Adapted [9].

3.1.3 Cherenkov Radiation

The observation of electromagnetic showers allows to draw conclusions about the energy and the direction of the primary photon. Due to the fact, that the electrons and positrons of the shower emit Cherenkov radiation, it is possible to observe an electromagnetic shower by detecting the Cherenkov radiation.

A charged particle emits Cherenkov radiation, when it moves through a dielectric medium of refractive index n with a velocity v greater than the speed of light c/n in that medium. β is the relation between the velocity v of the particle and the speed of light in vacuum c.

$$v = \frac{c}{n} \leq \beta c \tag{3.5}$$

The origin of Cherenkov radiation are molecules in the medium, which are polarised by the charged particle and become electric dipoles. Because of time variations of the dipole field, electromagnetic radiation is emitted. If the velocity of the charged particle is smaller than the speed of light, $v < c/n$, the dipoles are generated symmetrically around the trajectory of the particle. The dipole field integrated over all polarised molecules is zero and thus, no electromagnetic radiation is emitted. But if the particle velocity exceeds the speed of light in the medium, $v > c/n$, the symmetry is broken. This leads to a non-vanishing dipole field, which emits Cherenkov radiation [15].

The emission of Cherenkov radiation is described geometrically by a “shock wave” behind the superluminal particle. In Figure 3.3, the geometric representation of the emission of Cherenkov radiation is shown. The particle travels a distance vt in the time t, whereas the wavefront covers a distance of ct/n at the same time. Therefore, the wavefront of the particle is emitted under a specific angle θ to the trajectory of the particle, which depends on the velocity v of the particle as well as on the refractive index n of the medium (cf. Equation 3.6). The cone of Cherenkov radiation under that angle is denoted as Cherenkov light pool [9, 16].

$$\cos\theta = \frac{c}{nv} \tag{3.6}$$

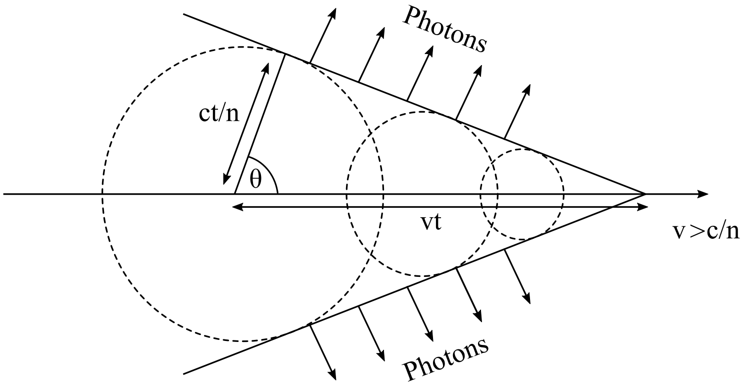

Figure 3.3: Geometric representation of the emission of Cherenkov radiation. The particle travels a distance vt in the time t, whereas the wavefront covers a distance of ct/n at that time. Hence, the wavefront of the particle is emitted under an angle θ to the trajectory of the particle. Adapted [16].

3.2 Imaging Atmospheric Cherenkov Technique

Like already stated at the beginning of this chapter, it is possible to measure cosmic gamma-rays by detecting Cherenkov radiation of electromagnetic showers initiated by a gamma-ray. The emitted Cherenkov photons form a light pool with a radius of about 200 m on the surface of the earth [17]. To detect these photons, the Cherenkov telescope has to be located inside the Cherenkov light pool as shown in Figure 3.4.

Cherenkov telescopes measure light by using cameras, which consist of matrices of photo multiplier tubes (PMTs). These cameras are mounted in the focal plane of a large reflector. To reconstruct the direction of the air shower, a set of multiple telescopes is used. By means of multiple telescopes, the shower can be measured from different points of view, which is illustrated in Figure 3.4.

By using the IACT, it is possible to determine the arrival direction of the Cherenkov light. This helps further to gain knowledge about the position of the celestial source of the gamma-ray. The intensity of the image obtained with the telescopes is informative about the energy of the incident gamma-ray, because the number of Cherenkov photons emitted in electromagnetic cascade is correlated to the energy of the primary photon. The shape of the image gives an indication about the nature of the primary particle of the shower, which can be either an electromagnetic or a hadronic particle. Thus, it is possible to separate showers initiated by cosmic rays from showers initiated by gamma-rays of a cosmic gamma radiation source. This is important to reduce the cosmic background, which is formed by detected hadronic showers [18, 19, 20].

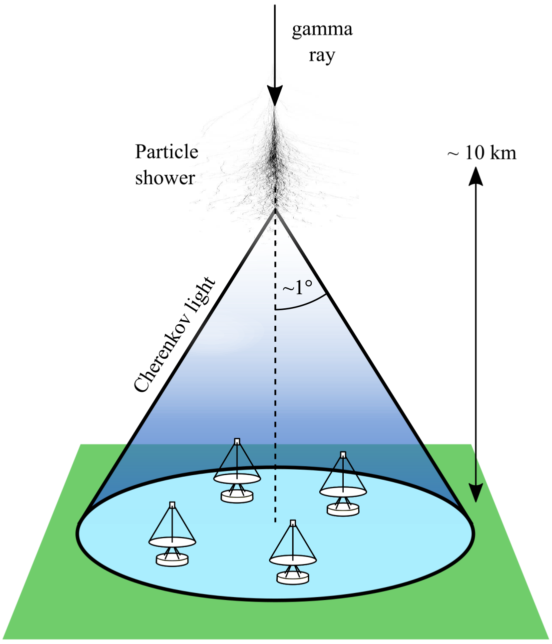

Figure 3.4: Cherenkov telescope array detecting Cherenkov light from a particle shower. The telescope has to be located inside Cherenkov the light pool. Adapted [18, 21].

3.2.1 High Energy Stereoscopic System

For this thesis, data obtained by the High Energy Stereoscopic System (H.E.S.S.) as input for the simulation of gamma-ray sources was used. In this subsection, a brief introduction to the telescope system is given. H.E.S.S. is a system of Imaging Atmospheric Cherenkov Telescopes located in Namibia, near the Gamsberg mountain at an altitude of about 1800 metres above sea level. It is named after the Nobel laureate Victor Hess and is used to examine cosmic gamma-rays within the energy range from 10s of GeV to 10s of TeV [18].

The telescope system consists of five telescopes (cf. Figure 3.5). The four smaller ones have been operating since December 2003 (H.E.S.S. I). The larger telescope in the middle (CT5, H.E.S.S. II) went into operation in July 2012. CT5 is with a total mirror area of $614\,\mathrm{m}^2$ the largest optical telescope in the world. The data as an input for the simulation was obtained with the small telescope and therefore the focus is only on the small telescopes. Each of them has a camera consisting of 960 PMTs (each PMT represents a pixel), which are mounted in a hexagonal order. The camera is divided in 38 trigger-sectors. The trigger-sectors overlap each other and consist of 64 PMTs. When more than four pixel measure a signal in one sector, the camera is triggered. Thereby, the night sky background is reduced. Another trigger, the coincidence trigger, makes sure that only events are stored if at least two telescopes trigger within a certain time interval [18, 22].

For the observation of an object the so-called “wobble mode” is used. The telescope does not point directly to the target, but uses an offset of ±0.5° to the source. By doing this, it is later possible to estimate the background and to subtract it. Moreover, the “wobble mode” reduces systematics in the data taking [21, 22].

Figure 3.5: The H.E.S.S. Telescope Array in Namibia consists of five telescopes, four small ones and a large one in the middle. Clementina Medina/Irfu-CEA [18].

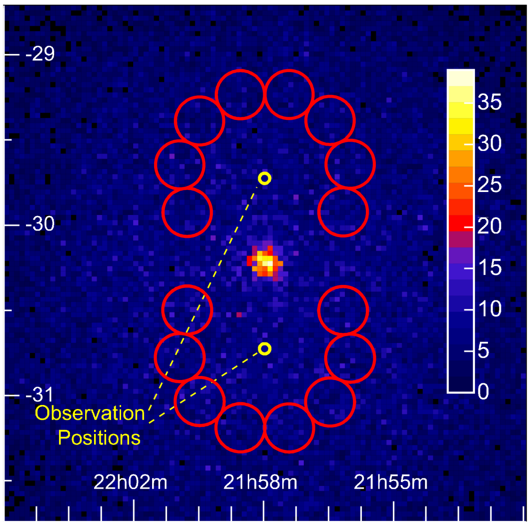

Figure 3.6: Schematic sketch of the data taking of the background (red circles) in the wobble mode around the observation position with an offset of ±0.5° in the direction of the declination to the source [23].

3.2.2 H.E.S.S. Standard Analysis

To cross-check the results, the H.E.S.S. Collaboration uses different analysis techniques [22]. In this subsection one of these techniques, the so-called H.E.S.S. Standard Analysis, is presented. For this analysis technique the observed images of the telescope are first "cleaned" by a two-stage tail-cut procedure. In this process all pixels with an intensity below 5 p.e. are neglected. An intensity of 5 p.e. corresponds to a signal of five incident photons. Furthermore, a pixel with an intensity below 10 p.e. is only kept when the intensity of a neighbour pixel is above 10 p.e. In Figure 3.7, a gamma-like event detected by the four small telescopes of H.E.S.S. is shown. The elliptical form of the shower can be clearly seen.

After that, the shower image is parameterized by an ellipse by using the Hillas parameters. The Hillas parameters are the *size* of the shower, which corresponds to the intensity of the detected light, its *length* and *width* and the *distance* between the centre of the shower and the camera centre. The orientation of the ellipse is specified by the angle α between the major axis and the line defined by the centre of the camera. In Figure 3.8 (a) the parameterisation of a shower image is shown.

For further analysis, several cuts, i.e. limitations on the range of value, are applied on these parameters. The three most important are:

- Size cut:

  The shower must have a minimal *size*. As a result, images which are not well reconstructed are eliminated.

- Distance cut:

  Only images are kept with a *distance* smaller than a certain threshold. Thus, images which are truncated at the edge of the camera are sorted out.

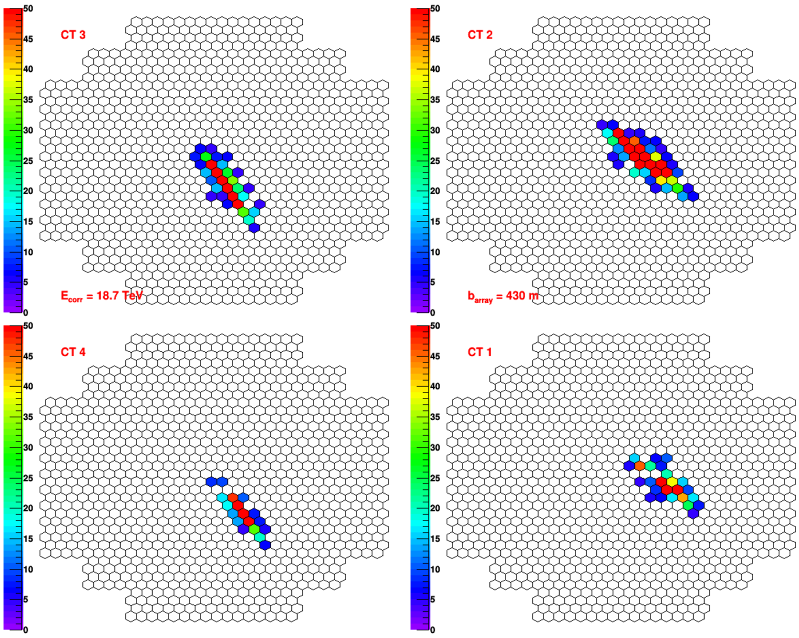

Figure 3.7: Gamma-like event detected by the four small telescopes of H.E.S.S. The colour scale shows the number of measured photons per pixel. The elliptical form of the shower is clearly visible.

- Mean-reduced scaled-width (MRSW) and length (MRSL) cut:
  The MRSW is calculated from the measured *width* of the shower and its expected width, determined by a simulation. The same applies to the MRSL for the *length* of the shower. Hence, the MRSW and MRSL parameters describe the mean value of the difference in standard deviation of width or length of a simulated gamma-ray event. Due to the fact that hadronic shower events have usually a longer and wider shape as gamma-ray events, it is possible to distinguish between gamma events and the cosmic background.

For the stereoscopic reconstruction of an event, at least the images of two telescopes have to pass the size cut and the distance cut. Then it is possible to identify the incident direction of the primary photon. Therefore, the intersection of the major axis of the elliptical shape of the gamma-ray events of at least two telescopes is determined. The intersection represents the initial direction of the shower and hence, the initial direction of the gamma-ray [20]. In Figure 3.8 (b), the principle of the reconstruction of the shower direction is sketched.

As stated above, there are other analysis techniques utilised besides the Standard Analysis. The data used as input for my simulation was analysed with the Model++ Analysis. This technique is based on the comparison of observed shower images to a semi-analytical model of the shower. Thereby, for example the asymmetry of the shower form, which is not a perfect ellipse, is taken into account. The Model++ Analysis is more complicated and needs more computing power than the Standard Analysis, but it provides also better angular resolution

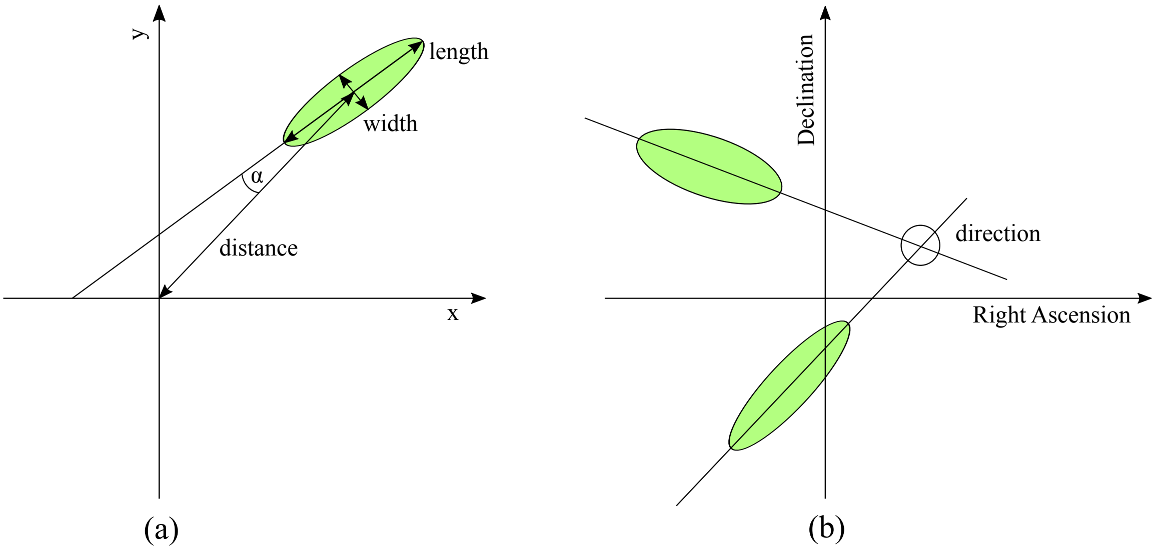

Figure 3.8: (a) The Hillas parameters of a shower parametrisation are the size of the shower, the length and width, the distance to the centre of the camera and the angle α between the major axis and the line defined by the camera centre. The x-axis and the y-axis define the image plane in the camera coordination system. (b) Principle of the reconstruction of the shower direction. Adapted [22].

[22].

After passing the above cuts, the detected events of an observed sky region are plotted in a so-called "skymap", a two dimensional histogram with the right ascension in units of deg on the x-axis and declination in units of deg on the y-axis. In an ideal observation, the events of a point source would be pinpointed in a single point of the skymap. In reality, the point source signal is broadened due to uncertainties on the original direction of the detected events. There is only a certain probability that the position of an event and its initial direction coincide. The point spread function (PSF) describes these uncertainties. Furthermore, the angular resolution and the accuracy of position determination of a point source are defined by the PSF [22].
The PSF is the limit of the resolution of an observation. But there are ways to bypass this limit by applying the technique of deconvolution to the skymap of an observed source. In the next chapter this technique of deconvolution is explained.

4 Deconvolution Algorithms

The concept of convolution can be found in many different fields of science, for example in optics, acoustics and signal processing, but also in the area of astrophysics. The convolution of two functions $f, g \in \mathcal{L}(\mathbb{R}^n)$ is defined as

$$(f * g)(x) \coloneqq \int_{\mathbb{R}^n} f(\tau) g(x - \tau) d\tau. \tag{4.1}$$

In Figure 4.1, the convolution of two Gaussian functions is shown. When a telescope observes a light source, the resulting image represents a convolution of the function which represents the actual source (hereafter referred to true source image) and the function of representation, which reflects the influence of the telescope on the measured data.
Deconvolution is the reverse process to convolution and can be performed with deconvolution algorithms. Those are widely used in the area of signal processing and image processing. They

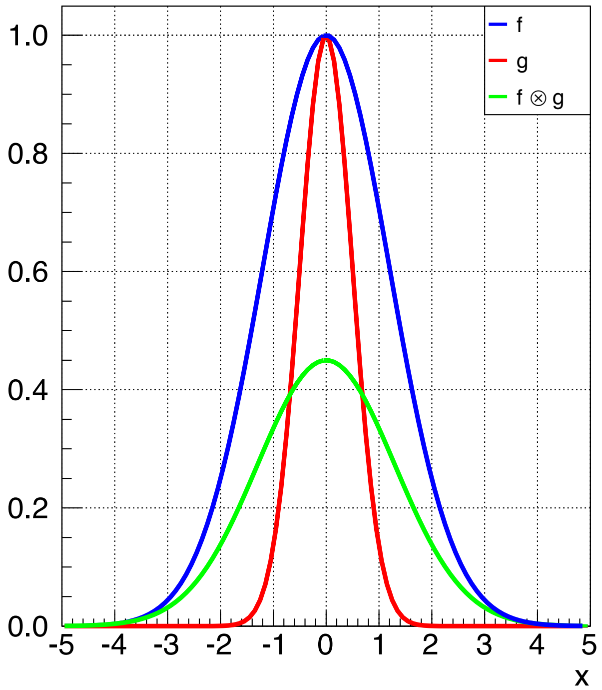

Figure 4.1: The convolution of two Gaussian functions.

help to improve the measured data and to restore the original image of an object from the measured image, which is affected by the properties of the measuring device. In the following, the idea of deconvolution analysis for astronomical images is introduced. Afterwards the two deconvolution algorithms which are used in this thesis are presented.

The astronomical image *I(x,y)* observed by a Cherenkov telescope with the right ascension (RA) on the x-axis and the declination (Dec) on the y-axis is assumed to be a two dimensional, discrete probability function [24]. A probability function of a sample is a function which assigns a certain likelihood to every event in that sample [25]. The probability function of an astronomical image $I(x,y)$ is defined as

$$I(x,y) = A(x,y)(O \otimes P)(x,y) + A(x,y)B(x,y). \tag{4.2}$$

$(O \otimes P)(x,y)$ is the convolution of the probability function of the true source image $O(x,y)$ and the point spread function (PSF) $P(x,y)$. $A(x,y)$ in Equation 4.2 is the probability function of the camera acceptance over the field of view. The camera acceptance has to be taken into account due to the fact that the measurement properties of the camera are not equal over the whole field of view of the camera. The PSF describes the influence of the function of representation of a Telescope to the image of a point source. The noise term $B(x,y)$ includes the background of the VHE γ-ray domain [24, 26].
The convolution of a true source image and the PSF is called *excess*-map, to which the algorithm is applied. To derive the *excess*-map, first the estimated background *(A(x,y)B'(x,y))* has to be subtracted from the image *I(x,y)*. Next, the obtained image has to be corrected by the acceptance over the field of view.
Thus, applying a deconvolution algorithm requires the knowledge of the PSF. Under this assumption it is possible to recover the original source image [26].

4.1 Richardson-Lucy Algorithm

The Richardson-Lucy algorithm (RCL) is an iterative Bayesian-based algorithm. Bayes's Theorem for two events A and B and the condition that the probability $p(B)$ for the event B is positive is defined in Equation 4.3. A represents the unknown information of the true source image and B the information of the *excess*-map, which is already known. Using Bayes's Theorem in Equation 4.3, one can make an estimation of $p(A)$ [27].

$$p(A \mid B) = p(A)\frac{p(B \mid A)}{p(B)}, \tag{4.3}$$

$p(B \mid A)$ is the conditional probability of an event B given event A. The algorithm is intended for a Poisson distributed background which converges to the maximum likelihood solution. As already stated, it is applied to a discrete probability-frequency function, which describes the degraded image E(*excess*-map) as the convolution of the original image O and the PSF P [24, 28]:

$$E = (O \otimes P)(x,y) = \sum_{n_x,n_y=1}^{N_x,N_y} O\left(x_{n_x}, y_{n_y}\right) \times P\left(x - x_{n_x}, y - y_{n_y}\right). \tag{4.4}$$

Originating from Equation 4.3 the deconvoluted image of the $(n+1)$-th iteration $O^{n+1}(x,y)$ is expressed by

$$O^{n+1}(x,y) = \left[\frac{E(x,y)}{P \otimes O^n(x,y)} \times P^{\intercal(x,y)}\right] O^n(x,y). \tag{4.5}$$

$P^{\intercal}(x,y)$ denotes the transposed PSF. The starting point of the first iteration $O^0(x,y)$ is assumed to be the uniform distributed using Bayes's postulate [24].
While using the RCL, one has to be aware of its disadvantages. As for other iterative deconvolution techniques, statistical fluctuations can be interpreted as real structure for sources with low significance. These fluctuations are called artefacts. With increasing number of iterations and decreasing significance of the structure the artefacts are growing, especially at the edges of the image. At a specific iteration number the negative influence of the artefacts is too high. A further deconvolution step would then be useless. Therefore, it is indispensable to study the behaviour of the RCL on different structures and significances by using simulated data. Simulations have the advantage that one can compare the deconvoluted image with the model image [26].

For this thesis, a C++-program written by Sebastian Heinz for the RCL deconvolution was used [22].

4.2 Maximum-Entropy Algorithm

Besides the RCL algorithm, the Maximum-Entropie algorithm (ME) is utilised to restore astronomical images. It is based on the method of maximum entropy and uses the Bayesian formulation as well as the RCL. The ME assumes that the probability distribution which reflects best our current knowledge about the available prior data is the probability distribution with the largest entropy. The principle of this ME method is that the prior data is "testable". This constraint means that it is possible to make a statement about the falsity or verity of the data [29]. The entropy S is defined as

$$S(\vec{p}) = -\sum_{i=1}^{L} p_i \log p_i \tag{4.6}$$

with $p_i (i = 1, 2, ..., L)$ the best set of proportions for a hypothetical probability function h. One can assume that the distribution h is positive and additive, which is applicable for many distributions used in science [27, 29]. With the measure m_i assigned to every cell i, the entropy can be written in the following form:

$$S(h) = \sum_{i=1}^{L} (h_i - m_i - h_i \log(h_i/m_i)) \tag{4.7}$$

The global maximum of the entropy can be found at $h = m$. At this point the deviation of h from the assigned measure m is minimal and the entropy is maximal. At the maximum entropy, one has the *maximal information* of the prior data set [27, 29].

For this master thesis, the MemSys5 package for maximum entropy analysis is used. The package has been developed by Maximum Entropy Data Consultants Ltd. and is written in FORTRAN 77.

5 Simulation of Gamma-Ray Images

In the last chapter two deconvolution algorithms were introduced, which use different approaches for deconvolution and behave differently. The question is what improvement they achieve for the analysis of an astronomical image. To study this, simulations of gamma-ray sources are used. A simulation has the advantage that the original source morphology is known. Therefore it is possible to compare the deconvoluted image to the true source morphology, which is in not possible for real data. Other advantages are that the PSF is exactly known and that different types of source morphologies can be studied.

In this chapter, the simulation used in this thesis will be discussed. First, the simulation of a the gamma-ray image of a point source will be described, which is the easiest case. Starting from the point source later on also the simulation of gamma-ray images of extended sources like a ring-shaped source or a Gaussian-shaped source will be presented.

5.1 Point Source

The structure of the simulation of the gamma-ray image is presented in Figure 5.1. Each part of the simulation is designated with a number. These designations are used for further explanations of the different parts of the simulation.

In the beginning of the simulation of a gamma-ray image one has to choose the model, i.e. the morphology of the source. In the case of a point source, the source model is a skymap with only one single pixel with a bin content different from zero (cf. Figure 5.2 (a)). But in reality, the camera does not observe a point but an extended source due to the broadening effects of the measurement equipment, which are described by the PSF (cf. Figure 5.2 (b)). The PSF used in the simulation is taken from the analysis of the supernova remnant RX J1713.7-3946 [23]. In Figure 5.3, the θ^2-distribution of the PSF of the analysis is shown. The θ^2-distribution of a skymap is its integral representation with regard to N_{bin} small cycles around the centre of the skymap. N_{bin} is the number of bins in the one-dimensional histogram of the θ^2-distribution. The PSF was fitted with a Landau distribution and after that filled into a skymap. The two-dimensional skymap of the PSF was used in the simulation and in the deconvolution.

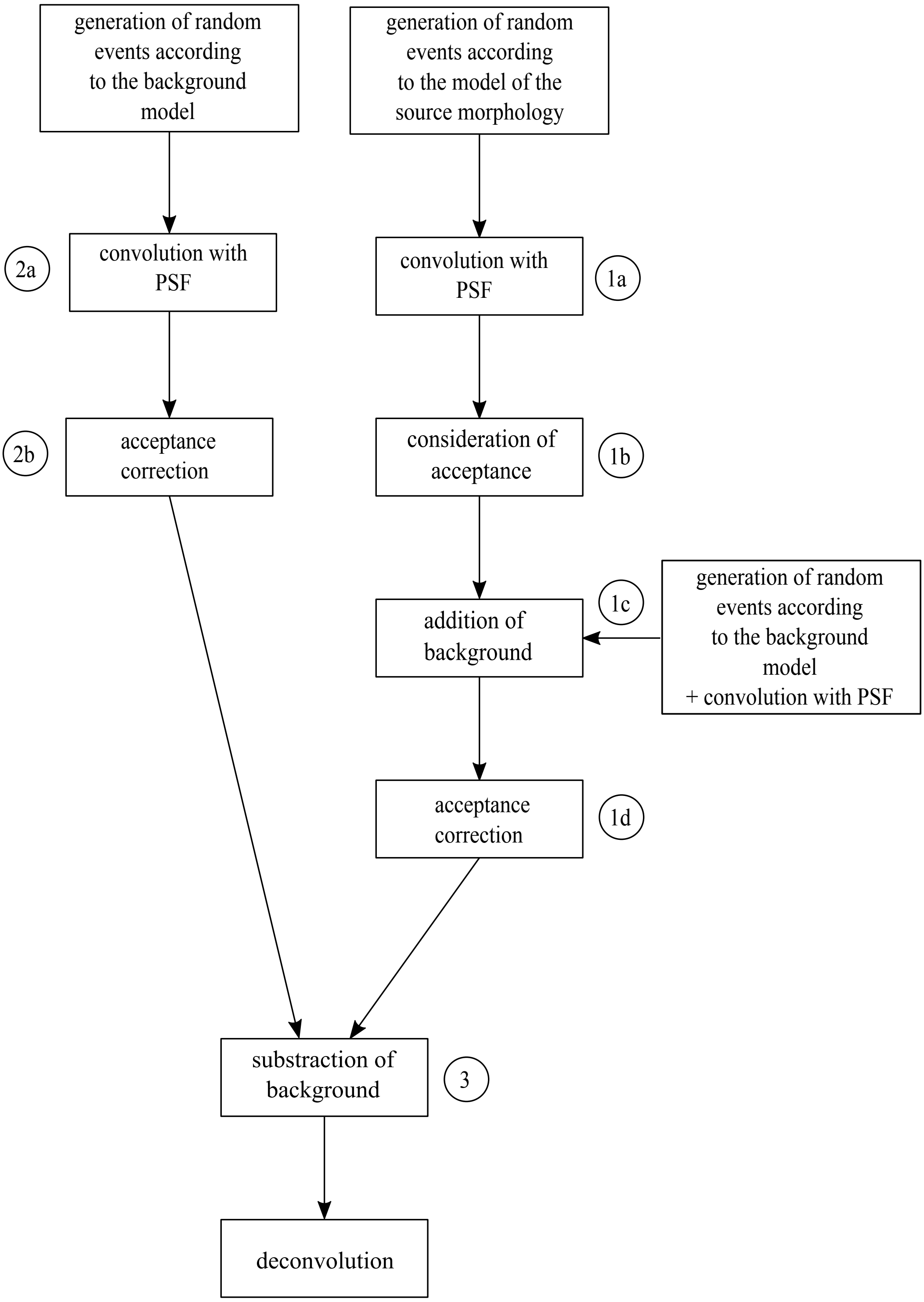

Figure 5.1: Sketch of the structure of the simulation of a gamma-ray image. Each part of the simulation is designated with a number, which is used to explain the structure of the simulation.

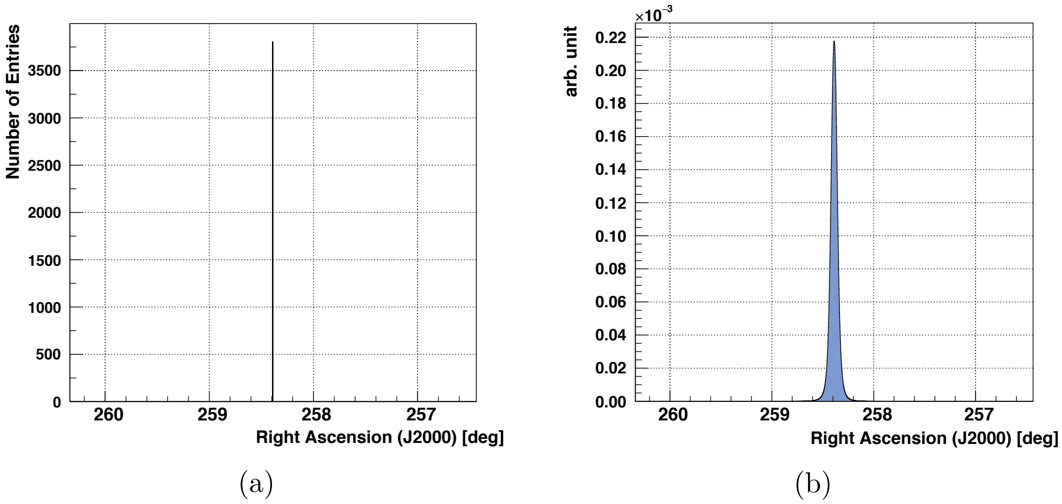

Figure 5.2: (a) Slice in the direction of the right ascension through the centre of the skymap of a point source model. (b) Slice in the direction of the right ascension through the centre of the skymap of the two-dimensional PSF.

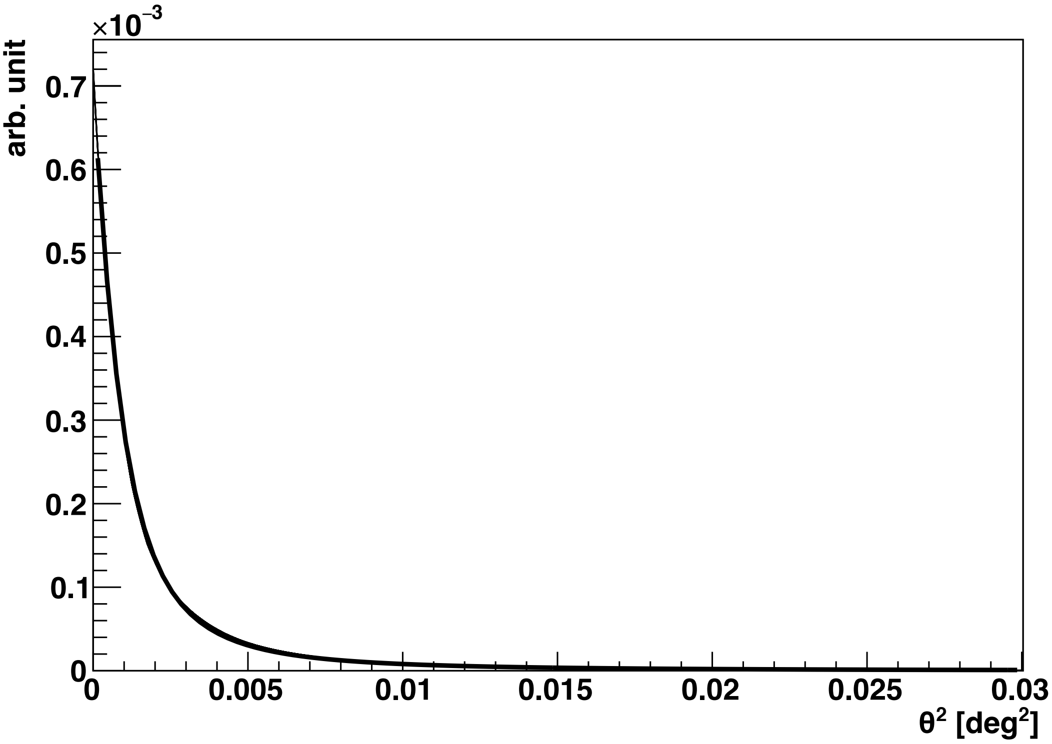

Figure 5.3: θ^2-distribution of the PSF from the analysis of RX J1713.7-3946 [23].

The first step of the simulation is to generate N_{ON} random events according to the point source model and to fill them into a skymap. N_{ON} is the number of events in the source without background. The generated skymap according to the source model is called simulated model map. The simulated model map simulates the fluctuations of the data taking in a real observation.
After that, the simulated model map is convoluted with the PSF. This process is also designated as “blurring” of the simulated model map with the PSF. The convolution of the simulated model map and the PSF corresponds to part 1a in the structure sketch of the simulation (cf. Figure 5.1). In Figure 5.4 (a), the convolution of the simulated model map and the PSF for N_{ON}=3806 is shown.

Due to the fact that the camera acceptance for real telescopes is not uniformly distributed, but drops at the edges, one has to take the acceptance distribution in form of a so-called acceptance map into account. The acceptance map for this purpose is also taken from the analysis of RX J1713.7-3946 [23] and shown in Figure 5.5 (a). Before using it in the simulation, the θ^2-distribution of the original acceptance map is polynomial fitted. The fit was done to avoid further artefacts. In Figure 5.5 (b), the fitted acceptance map can be seen. The term “acceptance map” will from now on refer to the fit of the θ^2-distribution of the original acceptance map.
The acceptance is considered in the simulation by the multiplication of every bin of the present simulated model of step 1a with every bin of the acceptance map. This part of the simulation corresponds to part 1b in Figure 5.1.

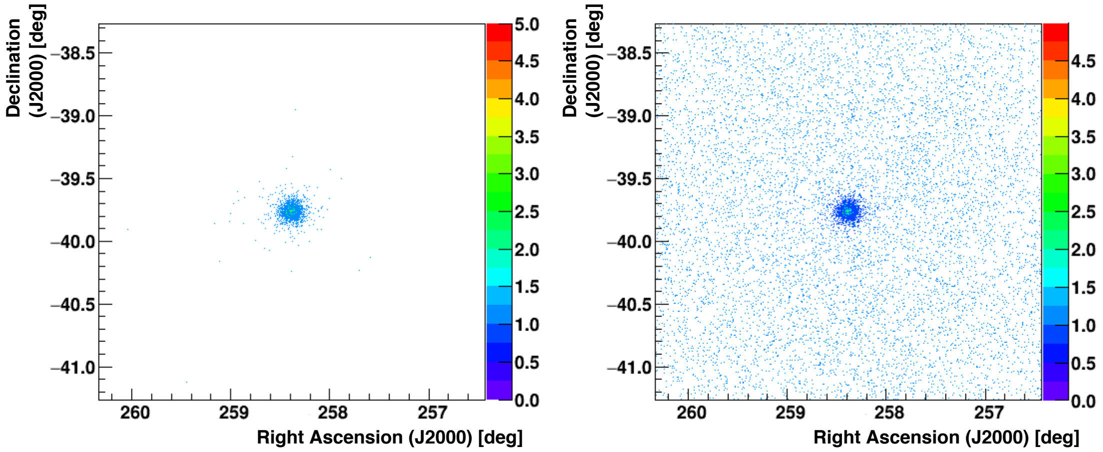

(a) (b)

Figure 5.4: (a) Convolution of the simulated model map and the PSF (step 1a in Figure 5.1). The number of events in the source without background is N_{ON}=3806.
(b) Addition of the background to the simulated model map (step 1c in Figure 5.1). The number of background events is N_{OFF}=8969.

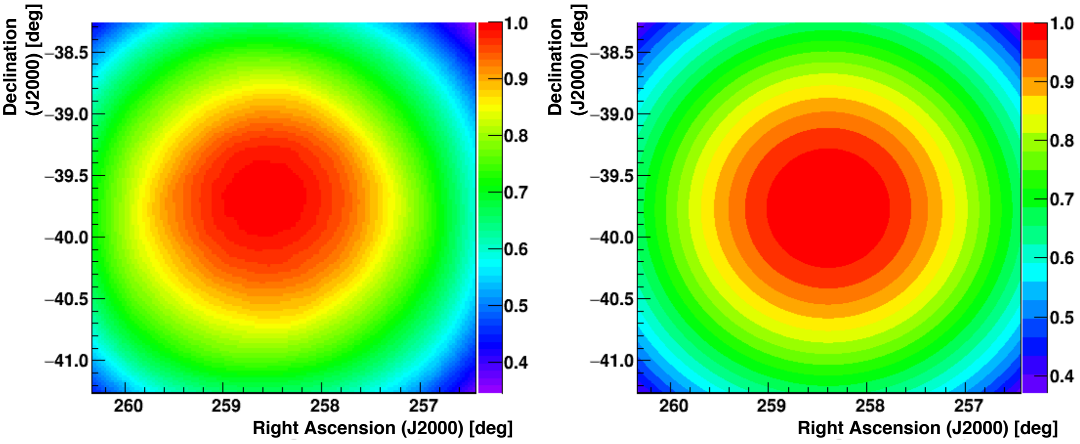

(a)

(b)

Figure 5.5: (a) Acceptance map from the analysis of RX J1713.7-3946 [23]. (b) The fitted θ^2-distribution of the original acceptance map in (a).

So far no background has been included in the simulation of the source image. To include fluctuations of the data taking, N_{OFF} random events are generated according to the acceptance map and filled into a skymap. N_{OFF} is the number of all background events in the skymap. The generated skymap in accordance with the acceptance map is hereafter called simulated acceptance map. The simulated acceptance map is convoluted with the PSF and after that added to the simulation. The adding of the background is illustrated by part 1c in Figure 5.1 and is shown in Figure 5.4 (b).

Part 1c of the simulation actually represents the astronomical image after the reconstruction of the shower direction of gamma events, observed by a virtual telescope. Because the camera acceptance affects the observed image, one has to apply an acceptance correction. For this purpose, the skymap of the simulation is divided by the acceptance map. Beforehand the acceptance map was normalised to one. This was done to make sure that bins in the simulation of the source image with 100% acceptance (that means within the centre of the skymap, around the source) are not changed by the division. The acceptance correction corresponds to part 1d in the simulation (cf. Figure 5.1).

The next step is now to subtract the background in order to obtain the *excess*-map. The deconvolution algorithms are later on applied to the *excess*-map. But before the background can be subtracted, it has to be simulated. The template of the background simulation is again the acceptance map.

First, αN_{OFF} random events are generated according to the acceptance map and filled into a skymap. The skymap is hereafter called simulated background map and is convoluted with the PSF. N_{OFF} represents again the number of background events and α is the nomination factor that takes the difference of the area and life time of the OFF-region and ON-region, which means the region where the source is located, into account. The life time is the acceptance corrected observation time of the telescope. By using αN_{OFF} random events, the background simulation follows the idea of background models like the multiple background model in a real measurement. Thereby the camera observes α different OFF-regions. The background is then determined by aligning the size of the OFF-regions to the size of the ON-region. In Figure 5.6, a sketch of the gamma-ray image of a point source is shown. The yellow circle around the source is the ON-region. The red circles are the α OFF-regions to determine the background. α is a number normally smaller than ten. For the simulation, α=7 was used.

The number of events in the simulated background map is aligned to a number of events in the simulation of the gamma-ray image, by dividing it by α. This alignment of the background, i.e. the OFF-regions, to the simulation, i.e. the ON-region, reduces fluctuations in real data-taking as well as in the simulation. This part of the simulation corresponds to step 2a in Figure 5.1.

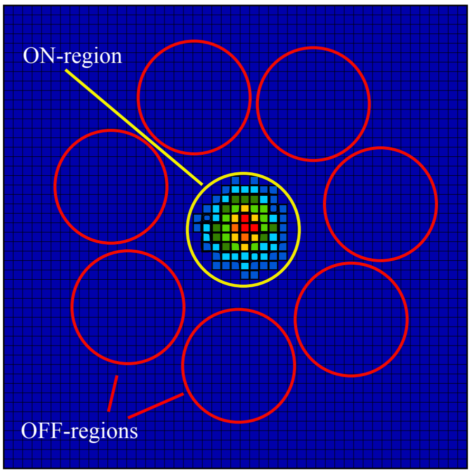

Figure 5.6: Sketch of the choice of α different OFF-regions. The OFF-regions are background regions around the source. The ON-region is the area in which the source lies. The background is determined by aligning the size of the OFF-regions to the size of the ON-region.

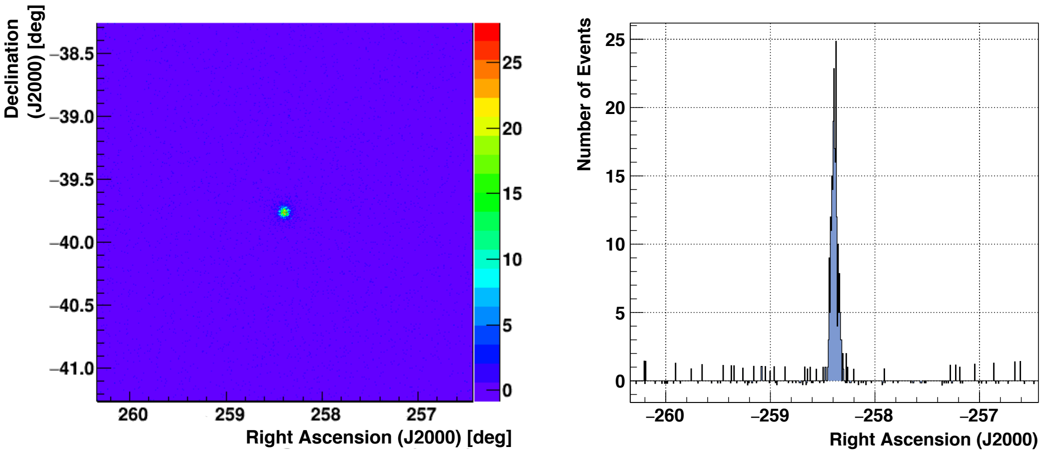

(a) (b)

Figure 5.7: (a) Simulated *Excess*-map of a point source. (b) Slice in the direction of the right ascension through the centre of the *excess*-map

.

As well as for the simulation of the gamma-ray image, also the simulated background map needs to be acceptance corrected, which is done by the division of the simulated background map by the acceptance map. This is illustrated by part 2b in the simulation sketch. In the final step the simulated background map is subtracted from the simulation to get the *excess*-map, which corresponds to step 3 in Figure 5.1. The resulting *excess*-map is shown in Figure 5.7. Now a deconvolution algorithm can be applied to the *excess*-map. The results of this deconvolution are presented and discussed in the next chapter.

5.2 Gaussian Morphology

In the universe, supernova remnants have extended morphologies instead of the point-like morphology explained in the previous subsection. To study the deconvolution of such sources, the simulation of gamma-ray images of extended sources is required. In this section the simulation on the example of a Gaussian source is presented.

Starting from the simulation the gamma-ray image of a point source, one has only to change the model of the source's morphology in the beginning of the simulation which corresponds to step 1a in Figure 5.1. In the case of a point source the model is a skymap with only one filled bin in the centre. For a Gaussian-shaped source however, a skymap with a two-dimensional Gaussian in the centre is used (cf. Equation 5.1). The nomination factor was α=1.5. In this way, it is also possible to adjust the size of the source by changing the 68%-radius d_{Gauss} of the Gaussian. In Figure 5.8 (a), the skymap of the source model of an extended point source for d_{Gauss}=0.1 deg is shown. In Figure 5.8 (b), the slice through the centre of the skymap in 5.8 (a) can be seen.

Similar to a Gaussian-shaped source, it is also possible to simulate gamma-ray images of ring-shaped sources, which is explained in the next section. The results of the deconvolution of a Gaussian-shaped source are discussed in Chapter 7.

$$f_{\mathrm{Gauss}}(x,y) = \frac{1}{2\pi d_{\mathrm{Gauss}}^2} \cdot \exp\left(-\frac{x^2+y^2}{2d_{\mathrm{Gauss}}^2}\right) \tag{5.1}$$

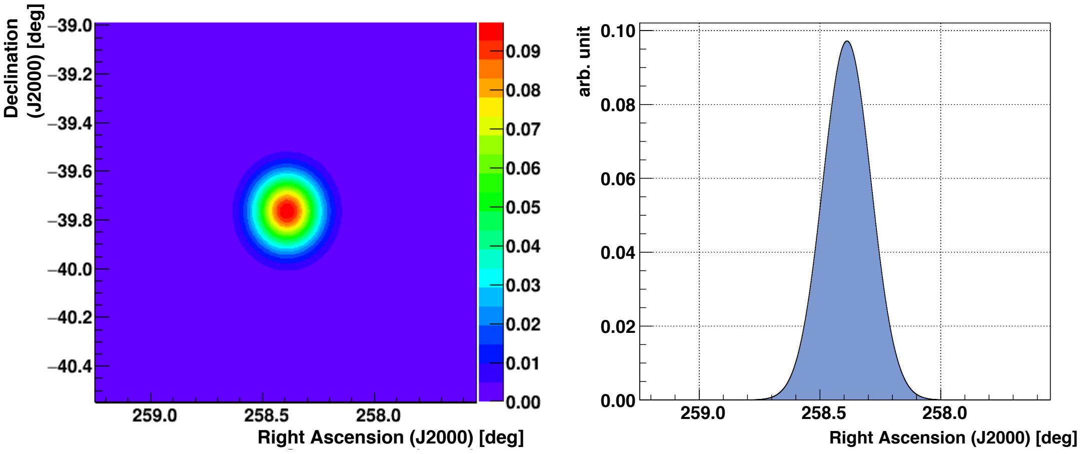

(a) (b)

Figure 5.8: (a) Skymap of the source model of a extended point source for a two-dimensional Gaussian with a width of d_{Gauss}=0.1 deg. (b) Slice through the centre of the skymap in (a) in the direction of the right ascension.

.

5.3 Ring Structure

Besides extended gamma-ray sources with a Gaussian morphology, there are also sources with a ring-shaped morphology like shell-type supernova remnants. One of the best known shell-type supernova remnants is RX J1713.7-3946. The correlation study with X-ray data presented in Chapter 8 for the supernova remnants RX J1713.7-3946 demonstrates an application of deconvolution algorithms.

To investigate the influence of deconvolution on the gamma-ray image of a ring-shaped source, it is appropriate to study it by means of a simulation. The simulation of a ring structure is implemented just as the simulation of a gamma-ray image of a Gaussian-shaped source. Instead of the Gaussian in the centre of the skymap, a model of a ring structure is used, defined by the function $f_{\mathrm{ring}}(x,y)$ in Equation 5.2. The nomination factor was α=1.5. The size of the ring is adjusted by six parameters: the inner radius r_{in} and the outer radius r_{out} of the ring, the steepness of the inner side and the outer side of the ring, k_{in} and k_{out}, and the position of the coordinates of the ring centre x_{c} and y_{c}. The first two parameters, r_{in} and r_{out}, were varied to study the influence of the size of the ring on the course of the relative error. The other four parameters have fixed values for all simulations of ring structures. The parameter values are presented in Table 5.1.

$$f_{\mathrm{ring}}(x,y) = \left[1+\exp\left(\frac{\sqrt{(x-x_{\mathrm{c}})^2+(y-y_{\mathrm{c}})^2}-r_{\mathrm{out}}}{k_{\mathrm{out}}}\right)\right]^{-1} \cdot \left[1+\exp\left(-\frac{\sqrt{(x-x_{\mathrm{c}})^2+(y-y_{\mathrm{c}})^2}-r_{\mathrm{in}}}{k_{\mathrm{in}}}\right)\right]^{-1} \tag{5.2}$$

In Figure 5.9 (a) the model of a ring structure $f_{\mathrm{ring}}(x,y)$ with an inner radius of r_{in} =0.1 deg and an outer radius of r_{out} =0.3 deg can be seen. In Figure 5.9 (b), the slice through the centre of the skymap in Figure 5.9 (a) in the direction of the right ascension is shown. The results of the deconvolution of a ring-shaped source are discussed in Chapter 7.

parameter	value [deg]
r_{in}	varied
r_{out}	varied
k_{in}	0.001
k_{out}	0.001
x_{c}	258.388
y_{c}	-39.7622

Table 5.1: Parameter values for the model of the ring structure $f_{\mathrm{ring}}(x,y)$, which is defined by Equation 5.2. The radii r_{in} and r_{out} of the ring structure were varied to adjust different sizes of the source. The other parameters were fixed in all simulations.

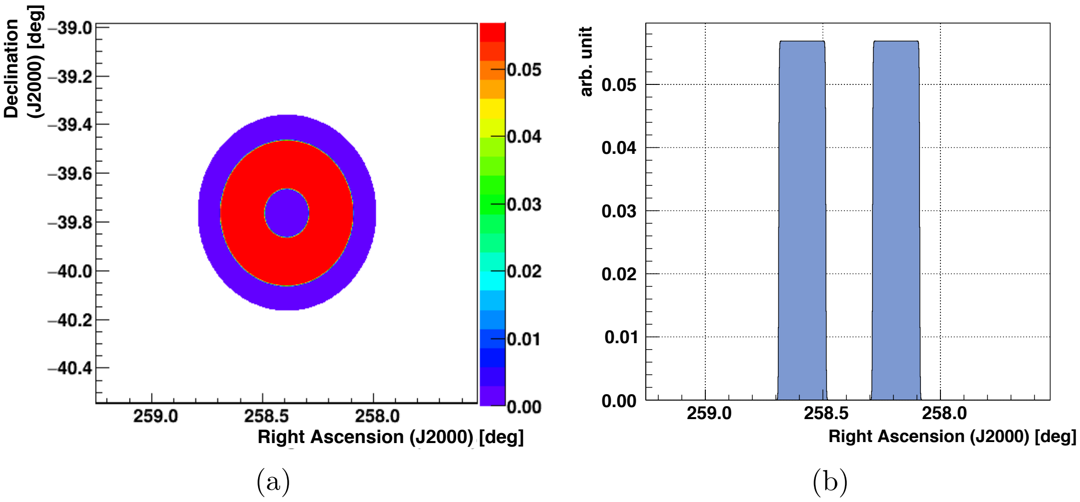

Figure 5.9: (a) Skymap of the source model of a ring structure with a inner radius of r_{in} =0.1 deg and a outer radius of r_{out} =0.3 deg. (b) Slice through the centre of the skymap in (a) in the direction of the right ascension.

.

6 Deconvolution of a Point Source

In the previous chapter, the simulation of gamma-ray images of sources with different morphologies was illustrated. The final result of the simulation led to the *excess*-map which is the starting point for the application of a deconvolution algorithm. In the framework of this thesis, two different deconvolution algorithms were utilised: the first one was the Richardson-Lucy algorithm which was used to investigate the influence of the deconvolution. The second one was the Maximum-Entropy algorithm which was planed to be used to compare its deconvolution results to the RCL. Due to a server update during this thesis, it was no longer possible to use the software of the ME. Thus, only some data of ME can be shown which was recorded before the update. Additional deconvolutions with the ME which were scheduled to be presented in this thesis, were unfortunately not possible.
In the following, the results of the deconvolution of a point source with the RCL are discussed. In the first part of this chapter, the behaviour of the so-called 68%-radius depending on the brightness of the source or the lifetime is examined. Afterwards, the focus is on the development of the relative error or the number of events in the *excess*-map during the deconvolution.

6.1 Study of the 68%-Radius of a Point Source

The main motivation to use deconvolution algorithms is to improve the resolution of the observed data. In the case of a point source, an improvement means that the width of the source becomes as small as possible to approximate the underlying morphology of a point source. The influence of the deconvolution on the width of the source is exemplary illustrated in Figure 6.1.

In order to measure the width of the source, the 68%-radius is used. The 68%-radius of a point source represents the resolution as well. The 68%-radius is defined as the radius in which 68% of all events are included. It is determined via the θ^2-distribution of the skymap of each iteration step of the deconvolution. The θ^2-distribution takes the bin content of a bin of a two-dimensional histogram and fills it into a one-dimensional histogram depending on the squared radial distance to the source centre. Afterwards, the integral from the source centre to each bin of the one-dimensional histogram is calculated. The bin centre of the bins in the one-dimensional histogram of the θ^2-distribution corresponds to the squared radial distance to the source centre. The integral is then compared for each bin to the integral over all entries of the one dimensional histogram to find the radius at which 68% of all events are included.
In Figure 6.2 (a), the θ^2-distribution of the 23th iteration of a deconvolution is shown. The source is located around a squared radial distance of $0\,\mathrm{deg}^2$ in the θ^2-distribution. Around a squared radial distance of $2.2\,\mathrm{deg}^2$ huge artefacts can be seen. These artefacts occur during

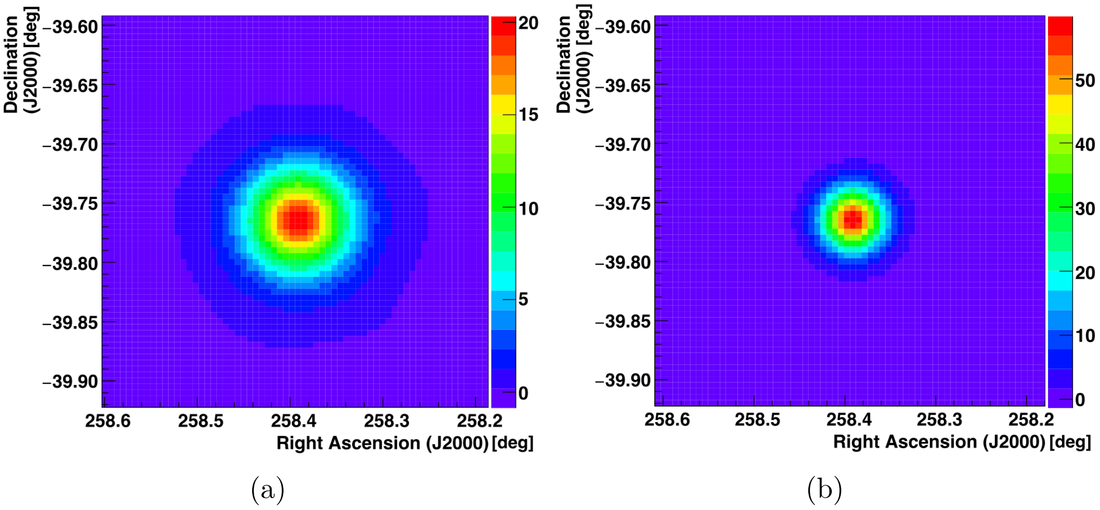

(a) (b)

Figure 6.1: (a) Skymap of the deconvoluted *excess*-map after two iterations. (b) Skymap of the deconvoluted *excess*-map after nine iterations. One can clearly see, that the deconvolution leads to a narrowing of the source, i.e. the 68% radius decreases.

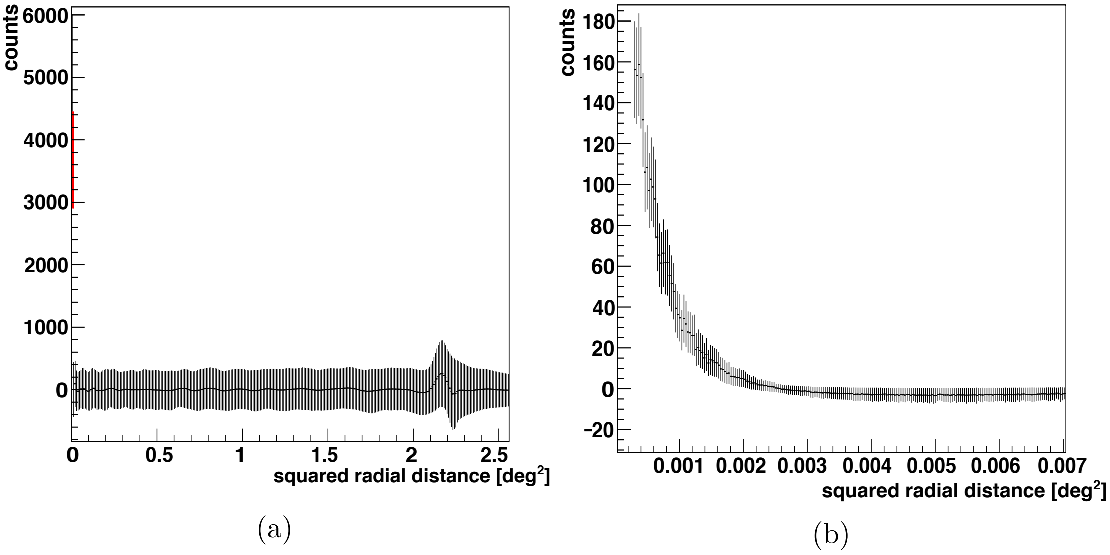

(a) (b)

Figure 6.2: (a) θ^2-distribution of the whole *excess*-map: the source is located around squared radial distance of $0\,\mathrm{deg}^2$ and marked in red. Between squared radial distances of $2.0\,\mathrm{deg}^2$ to $2.5\,\mathrm{deg}^2$, i.e. at the edges of the skymap, artefacts can be seen. (b) θ^2-distribution around the source. The range of the y-axis is limited to 180 counts, higher values are truncated to provide a clear overview of the θ^2-distribution for lower counts. It is sufficient to take the direct area around the source for the calculation of the 68%-radius into account.

the deconvolution at the edges of the skymap and increase with the number of iterations. If one regards the θ^2-distribution of the whole skymap for the determination of the 68%-radius, the artefacts would distort the result. Therefore, one has to consider only the area around the source as shown in Figure 6.2 (b).

Another important point is the binning, i.e. the size of the bins, of the one-dimensional histogram of the θ^2-distribution and its relation to the binning of the deconvoluted *excess*-map. In Figure 6.3, a schematic sketch of a skymap is shown. The yellow bin in the centre represents the underlying model of the morphology of a point source. The binning of the θ^2-distribution corresponds to the width of the coloured circles. Depending on the percentage of the bin area lying for example within the orange circle, the corresponding part of the bin content is filled into the orange bin in the one-dimensional histogram. The θ^2-distribution-binning, that means the width of the coloured circles, has to be small enough to provide a sufficient resolution to resolve the decrease of the 68%-radius during the deconvolution. On the other side, with a smaller binning the impact of the weighting of the area increases. The "real" shape of the θ^2-distribution of the examined skymap actually depends on the binning of the skymap, but it is affected by the binning of the θ^2-distribution. Furthermore, a smaller binning leads also to longer run times. One has to decide if a smaller binning of the θ^2-distribution in the area directly around the source really leads to a better resolution.
In this thesis a binning of the θ^2-distribution of $0.000032\,\mathrm{deg}^2$ was used. This bin size was chosen to guarantee a sufficient resolution of skymaps with a small binning. It was fixed for all calculations of the 68%-radius. The choice of the binning of the skymap and its influence on the 68%-radius is discussed later on.

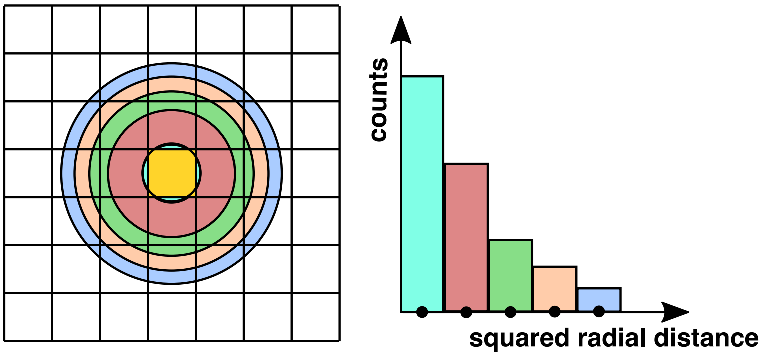

Figure 6.3: On the left side a schematic sketch of a skymap of a point source is shown. The yellow bin represents the point source, the width of the coloured circles the binning of the θ^2-distribution. The bin content of each bin of the skymap is weighted by the percentage of the bin area lying in one of the coloured circles. Depending on the weighting, it is filled in the one-dimensional histogram on the right side in respect to its squared radius to the centre of the skymap. The black dots in the one-dimensional histogram represent the bin centre, which defines the position of the bin for the calculation of the 68%-radius.

Significance

The brightness of a source is defined as the ratio between the source events (in reality these would be detected events originating from gamma photons) and background events (from cosmic radiation). The brighter the source, the more events are stemming from the source compared to the background. This definition corresponds to the term significance σ. In Equation 6.1 after [30] the number of ON-events N_{ON} (signal events without background) depends on the number of OFF-events within a fixed area around the source $N_{\mathrm{OFF,source}}$, the normalisation factor α and the significance σ. Source simulations with high σ contain more ON-events and thus, represent brighter gamma sources.

$$N_{\mathrm{ON}} = \frac{1}{2}\sigma^2 + 2\alpha N_{\mathrm{OFF,source}} + \sqrt{\frac{1}{4}\sigma^4 + \frac{8\sigma^2}{\alpha} N_{\mathrm{OFF,source}}} \tag{6.1}$$

In Figure 6.4 the dependence of the 68%-radius for point sources with different significances on the number of iterations of the RCL is shown. The lifetime is the acceptance corrected observation time and it is 25 h in this study. The data points are the mean values the 68%-radius of 20 simulations. The error is the standard error. In order to provide a clear overview of the presented data, every tenth iterations was plotted. Furthermore, for each significance the starting point is varied to avoid the overlap of the data points. Apart from that, the first iteration of the RCL, which actually corresponds to the uniform distribution as stated in Chapter 4, is neglected. Since the uniform distribution does not include the source morphology, the result of the first iteration is always significant worse (in the case of the 68%-radius higher) than the results of the following iterations. The first iteration in Figure 6.4 represents therefore the second iteration. This applies to all plots which are presented in context of the deconvolution of a point source.

The 68%-radius decreases with increasing number of iterations. It is significantly smaller than the 68%-radius of the PSF with 0.048 deg, which is the resolution of the undeconvoluted image. In addition, the 68%-radius is on average smaller for higher significances, as one can see in Figure 6.4. This is in line with the expectations since a source with higher significance has more events in the source area. Hence, it stands out better from the background. Moreover, it is apparent that the standard error decreases with increasing significance. The reason for that is the same as for the smaller 68%-radius: more events in the source area lead to a better-defined source shape and facilitate the deconvolution. Consequently the results of the 68%-radius of different simulations with a high significance do not vary as much as for a source with a lower significance.

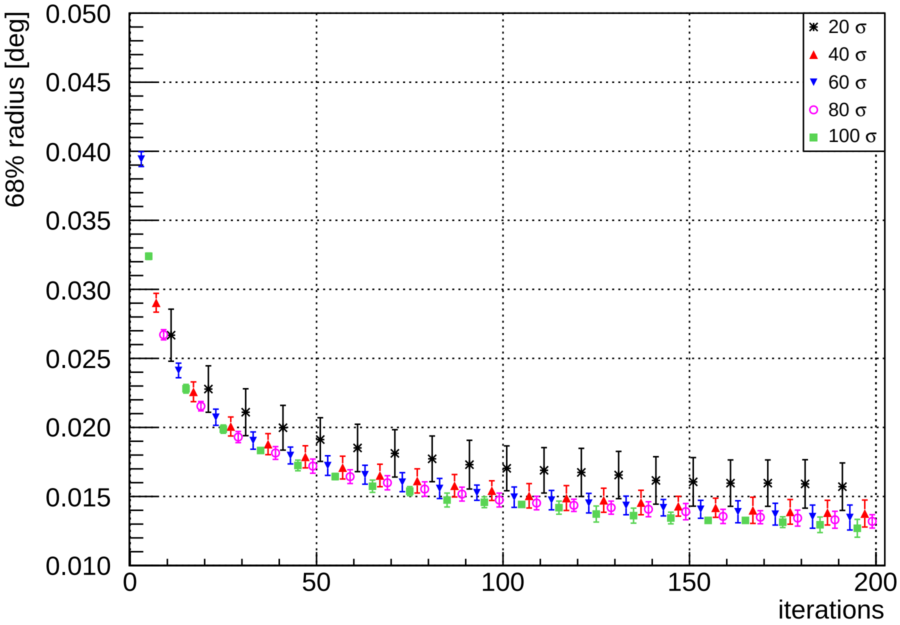

Figure 6.4: The 68%-radius as a function of the number of iterations for point sources with different significances. The data points are the mean values the 68%-radius of 20 simulations. The error is the standard error. In order to provide a clear overview of the presented data, every tenth iterations was plotted.

Lifetime

In a real observation the observation time indicates how long a source was observed. The lifetime is the acceptance corrected observation time as already stated in the previous paragraph. The longer the lifetime, the more events are measured, including gamma events as well as background events. The number of events used in this simulation originates from the already mentioned analysis of the supernova remnant RX J1713.7-3946 [23], for which the lifetime is known. Hence, different lifetimes can be adjusted by scaling the number of events of the analysis.

In the following, the impact of the lifetime on the 68%-radius is discussed. In Figure 6.5, the 68%-radius for different lifetimes depending on the number of iterations for a point source of 60 σ can be seen. The plotted data points are the mean values of 20 simulations for each iteration, the error is the standard error. Also here every fifth iteration was plotted.
As can be seen, the influence of the lifetime on the 68%-radius is quite small. The small difference for various lifetimes is significant smaller than the standard error on the mean value. The results can be explained by the influence of the lifetime on the simulation: the number of OFF-events in the source region $N_{\mathrm{OFF,source}}$ depends on the lifetime. Furthermore, the number of ON-events N_{ON} is calculated from $N_{\mathrm{OFF,source}}$ to obtain a significance of $60\,\sigma$. However, the different lifetimes only lead to a slightly different N_{ON}. Thus, one would not expect to see a

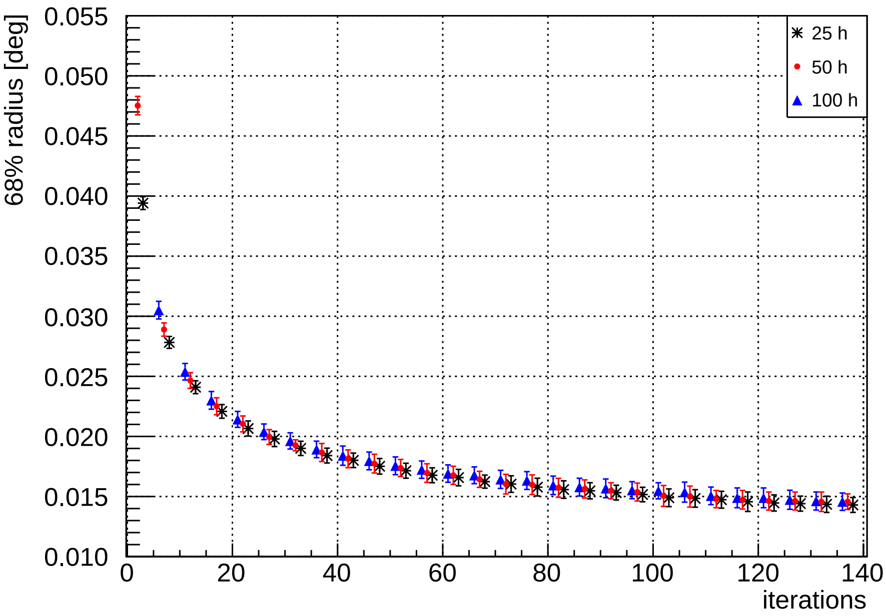

Figure 6.5: The 68%-radius as a function of the number of iteration for point source with different lifetimes. The significance of the sources is 60 σ. The error is the standard error of 20 simulations. Every fifth iteration was plotted.

significant difference for the behaviour of the 68%-radius. For the studies of the deconvolution of a point source a lifetime of 25 h was used if not stated otherwise.

Binning of the *excess*-map

An essential factor at the issue of how small the calculated value of the 68%-radius can become is the binning of the *excess*-map. The binning of the *excess*-map in the simulation is about 0.0013 deg. For a point source this value achieves the best result one can reach for the 68%-radius. But also if one would use this binning, it is not guaranteed to reach the smallest value in a fixed number of iterations. In practise, the time per deconvolution is limited and therefore also the number of iterations. However, finer binnings are stronger affected by statistical fluctuations. Therefore, the 68%-radius decreases slower during the deconvolution then in the case of a rougher binning. A finer binning does consequently not always lead to a better result.

Another striking aspect is the relation between the binning and the run-time of the calculation: the finer the binning, the higher the run-time. For example, a rebinning of 5 bins would lead to a 25-times faster calculation. So, it is promising to use some kind of rebinning. The term “rebinning” designates the combination of a group of bins to one bin. In the case of a rebinning of 5 (rebin 5), 25 bins are combined to one bin. Hence, the new bin is five times wider in the direction of the right ascension as well as in the direction of declination, i.e. the

rebin	bin width [deg] of right ascension	bin width [deg] of declination
-	0.0013	0.0010
2	0.0026	0.0020
5	0.0065	0.0050
10	0.013	0.010
15	0.020	0.015

Table 6.1: Different rebinnings of the *excess*-map with corresponding bin width in the direction of right ascension and the declination.

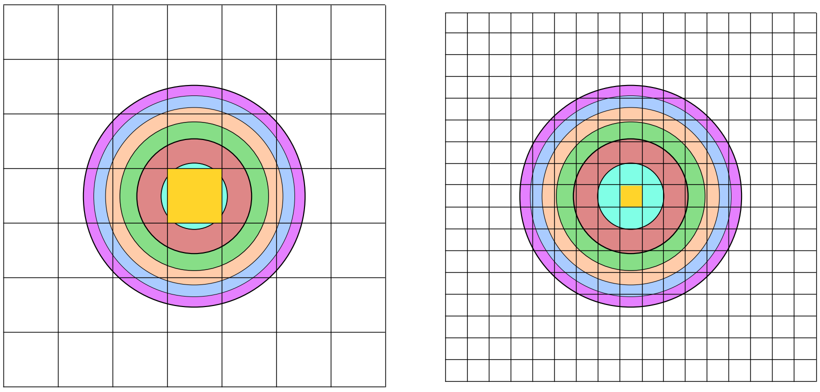

Figure 6.6: The left sketch shows the histogram of a point source model with rebin of 5, the right sketch the same histogram with a rebin of 2. The width of the coloured circles represents the binning of the θ^2-distribution, which is used to calculate the 68%-radius. The model of a point source is illustrated by the yellow bin in the centre.

rebinning of 5 leads to a twenty five times enlargement of the initial bin.

In Table 6.1, different rebinning with their corresponding bin width in respect to the bin width of the unrebinned *excess*-map are listed. In Figure 6.6, a sketch of a histogram of a point source model with a rebin 5 and a rebin 2 in respect to the unrebinned bin width of 0.0013 deg is shown. The yellow bin in the centre is the model of the point source. The coloured circles represent the binning of the θ^2-distribution, which is applied to determine the 68%-radius. As one can see, a finer binning like rebin 2 provides theoretically a better resolution and allows a smaller θ^2-distribution. In contrast, for a rougher binning like rebin 5 also a rougher binning of the θ^2-distribution would be sufficient. Though, in this study always the same binning of the θ^2-distribution was used, independent of the binning of the deconvoluted *excess*-map.
In Figure 6.7 the dependence of the 68%-radius on the binning of an *excess*-map of 60 σ for 1000 iterations is shown. The data points are the mean values of the 68%-radius of 20 simulations, error is the standard error. To provide a clear overview of the presented data, every 20th iterations was plotted.

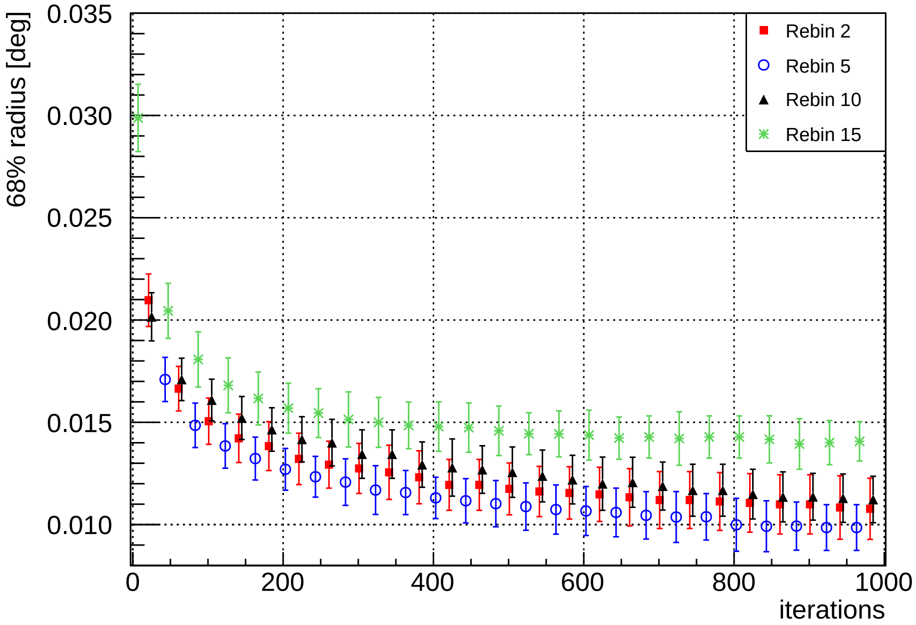

Figure 6.7: The 68%-radius as function of the number of iteration for different binnings of the *excess*-map of a point source. The significance of the sources is $60\,\sigma$. The error is the standard error of 20 simulations, the data points are the mean values of the 68%-radius of 20 simulations. To provide a clear overview of the presented data, every 20th iterations was plotted.

With a rough binning like rebin 15 the minimal possible value is reached quite rapidly in comparison to the finer binning. The smallest value can be determined with rebin 5. The 68%-radius with a smaller binning of rebin 2 decreases also continuously, but slower, than with rebin 5. Viewing Figure 6.7 it stands out that the errors for rebin 2 are larger than for rebin 5. This gives a hint to an explanation, why the rougher binning provides better results: a smaller binning is theoretically expected to provide a better resolution and hence, a smaller value for the 68%-radius. However, it includes also more fluctuations which are interpreted as signal. Hence, the 68%-radius decreases slower in the case of a finer binning.

In this thesis a rebinning of 5 was used for all further studies of the point source because it has a good resolution for the 68%-radius and it results into smaller run-times compared to finer binnings. In the study of the deconvolution of extended sources, which is presented in Chapter 7, a rebinning of 10 was used in consideration of the smaller number of reasonable iterations and the resulting lower resolution.

Comparison of both algorithms

Initially, the goal of this thesis was the comparison of the two deconvolution algorithms, which were introduced in Chapter 4. Unfortunately this was no longer possible after the software update. Nevertheless, some deconvolutions with the ME were already executed before the update.

For these deconvolutions an earlier version of the simulation was used. Therefore, the number of events was not defined over the lifetime with regard to the data file of RX J1713.7-3946. Instead, the number of all OFF-events of α OFF-regions $N_{\mathrm{OFF},tot}$ was adjusted to $N_{\mathrm{OFF},tot}= 8000$, which corresponds to an lifetime of 13.39 h. The lifetime was the only parameter which was changed compared to the other studies of the point source.

In Figure 6.8 the deconvolutions of a point source of 20 σ by the RCL and ME deconvolution algorithms are shown. The run of one single deconvolution for 1000 iterations by the ME takes two weeks, whereas the RCL needs for the same deconvolution less than half an hour. Due to the long run time of the ME, only one deconvolution was executed.

One can clearly see the steps in the behaviour of the 68%-radius in Figure 6.8. These steps originate from the binning of the θ^2-distribution. The comparison of the results of the RCL to the ME shows that the 68%-radius obtained by the RCL decreases faster. After 1000 iteration the deconvolution with the RCL achieved a smaller result of 0.012 deg for the 68%-radius than the ME with 0.013 deg. But it is possible that also the results of the ME would decrease further if the deconvolution would be executed with more iteration.

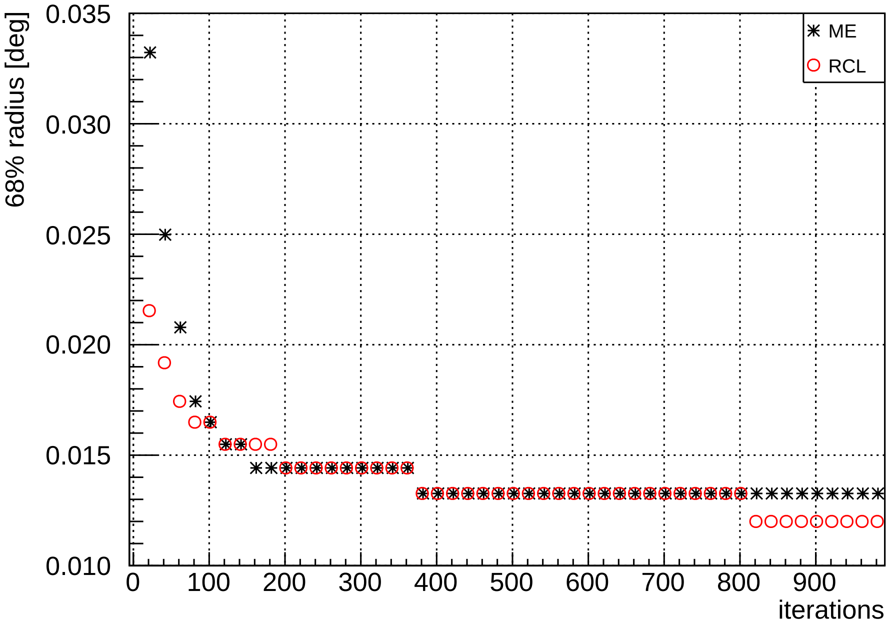

Figure 6.8: Deconvolution of a point source of 20 σ by the RCL and ME deconvolution algorithms. The plotted curve is the 68%-radius as a function of the number of iterations.

6.2 Study of the Relative Error of a Point Source

So far the development of the 68%-radius during the deconvolution was studied. Another interesting quantity is the relative error. It is of particular importance in the case of extended sources in Chapter 7. However, the relative error is first studied in the context of point sources. The relative error indicates how well the deconvolution matches to the model of the source. It is therefore, just as the decrease of the 68%-radius, a way to assess the question to what extent an iteration step of the deconvolution leads to an improvement of the gamma-ray image's resolution. The relative error is calculated according to Equation 6.2:

$$\left|\frac{\Delta z}{z_0}\right| = \sqrt{\frac{\sum_{i=1}(z_i - z_{0,i})^2}{\sum_{i=1} z_{0,i}^2}}. \tag{6.2}$$

Here $\left|\frac{\Delta z}{z_0}\right|$ denotes the relative error of a deconvoluted *excess*-map in relation to the source model. The bin content of a bin i of the deconvoluted *excess*-map is z_i, the bin content of a bin i of the source model is $z_{0,i}$. The sum over the squared bin content of all bins of the skymap of the source model is $\sum_{i=1} z_{0,i}^2$. The relative error was determined in an area around the source with a radius of 0.20 deg to the source centre, in which 99% of the area of the PSF is included. In Figure 6.9, the size of the 99%-radius of the PSF is illustrated by a withe circle in the bottom left corner.

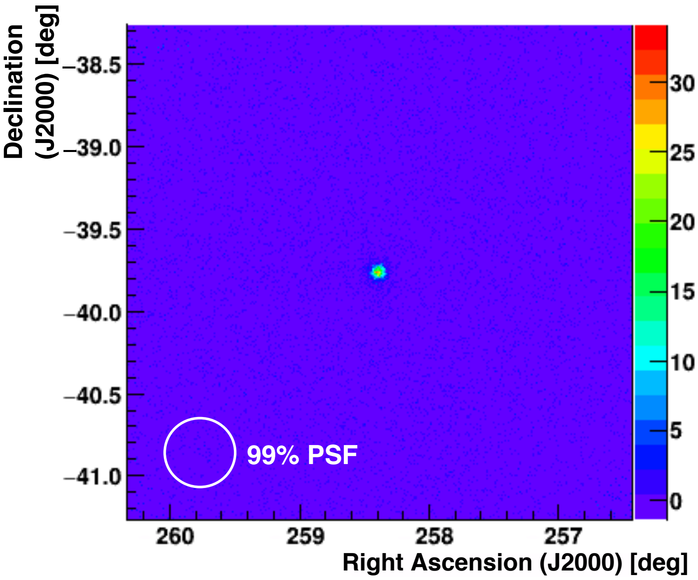

Figure 6.9: Skymap of the PSF with illustration of the size of the 99%-radius of the PSF as a white circle in the bottom left corner. The relative error is calculated within this radius around the source in the case of a point source.

Significance

In Figure 6.10 the relative error as a function of the number of iterations for different significances of a point source is presented. The error is the standard error of 20 simulations. In order to provide a clear overview over the presented data, every fifth iteration was plotted. One can see that the relative error decreases slowly and continuously. The reason for the small decrease is the fact that the deconvoluted *excess*-map is compared to a source model with only one filled bin. Therefore, it is clear that the relative error is quite high. Furthermore, the 68%-radius decreases with increasing number of iteration, i.e. the deconvoluted point source becomes narrower for higher significances. This dip can be explained in a similar way as in the study of the 68%-radius: a simulation with a higher significance contains more ON-events. Thus, the morphology of the source stands out better from the background.
Another striking feature in Figure 6.10 is the increase of the standard error with the number of iterations. If one looks at the single values for each simulation and each iteration, one sees that the simulations diverge during the deconvolution. Some simulations are closer to the model than other at beginning due to statistical fluctuations. During the deconvolution this initial difference develops further and is more pronounced with every iteration step. That means that the relative error of a simulation close to the model decreases faster than the relative error of a simulation which differs more from the model. The standard error just reflects this development by increasing with the number of iterations.
A similar behaviour of the standard error was not observed for the 68%-radius.

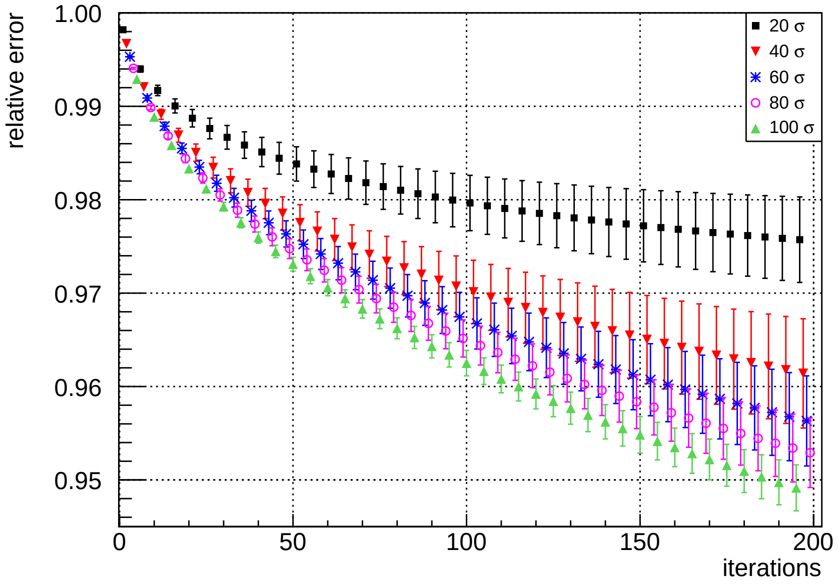

Figure 6.10: The relative error as a function of the number of iterations for point sources with different significances. The error is the standard error of 20 simulations. Every fifth iteration was plotted.

Binning of the *excess*-map

Besides the significance one can also study the relative error as a function of the number of iterations for a point source simulation with different binnings, which is shown in Figure 6.11. The error is the standard error of 20 simulations. In order to provide a clear overview over the data, every 40th iteration was plotted.

Once more the relative errors decreases continuously. Remarkable is the difference of the behaviour of the relative error for finer and rougher binning: for finer binning the relative error decreases slowly, for rougher binning the relative error drops off more rapidly. The reason for that is clear if one keeps in mind that a larger rebinning of the *excess*-map requires also a larger rebinning of the source model. Thus, the size of the source in the skymap of the source model, or to be more precise, the bin width is larger. At the same time the fluctuations within the deconvoluted *excess*-map are smaller since the *excess*-map is smoothed by the rougher binning. Hence, the difference between the deconvoluted *excess*-map to the source model becomes smaller.

Another notable feature is the increase of the relative error with growing number of iterations. The reason for that is the same as already explained in the last paragraph for the dependence on the significance: some simulations are closer to the model than other. The difference of the deviation to the model for the simulations develops further during the deconvolution, i.e. the difference between the simulations increases with every iteration steps and therefore also the standard error.

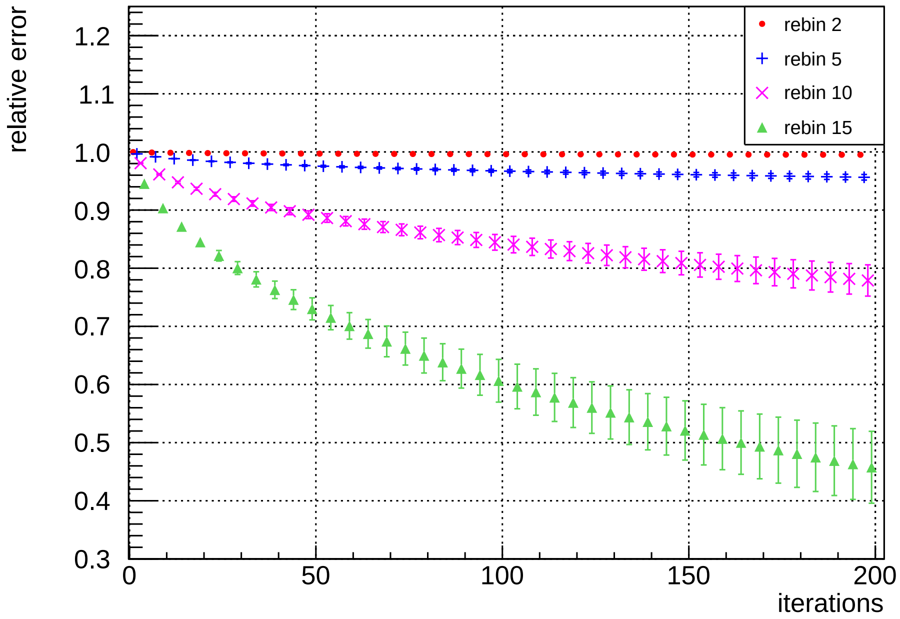

Figure 6.11: The relative error as a function of the number of iterations for different binnings of the *excess*-map of a point source. The significance of the sources is 60 σ.

6.3 Study of the Event Conservation of a Point Source

The 68%-radius and the relative error allow to judge to what extent the deconvolution improves the resolution of a point source. An important requirement of the application of a deconvolution algorithm is the fact that the algorithm does not influence the number of events in the *excess*-map. The RCL is an event conserving algorithm and fulfils the above stated requirement.

In Figure 6.12, the deviation of the event number during the deconvolution compared to the number of events of the undeconvoluted *excess*-map as a function of the number of iterations is shown. The deviation means the difference between the number of events of the deconvoluted *excess*-map to the number of events to the undeconvoluted *excess*-map normalised to the events of the undeconvoluted *excess*-map. The error is the standard error of 20 simulations.

The deviation during the deconvolution to the initial number of events is around 2%. For a smaller significance the behaviour is more variable and the error is larger than for a higher significance. Despite the small deviation can be concluded that the number of events is conserved during the deconvolution. Hence the requirement of the application is fulfilled.

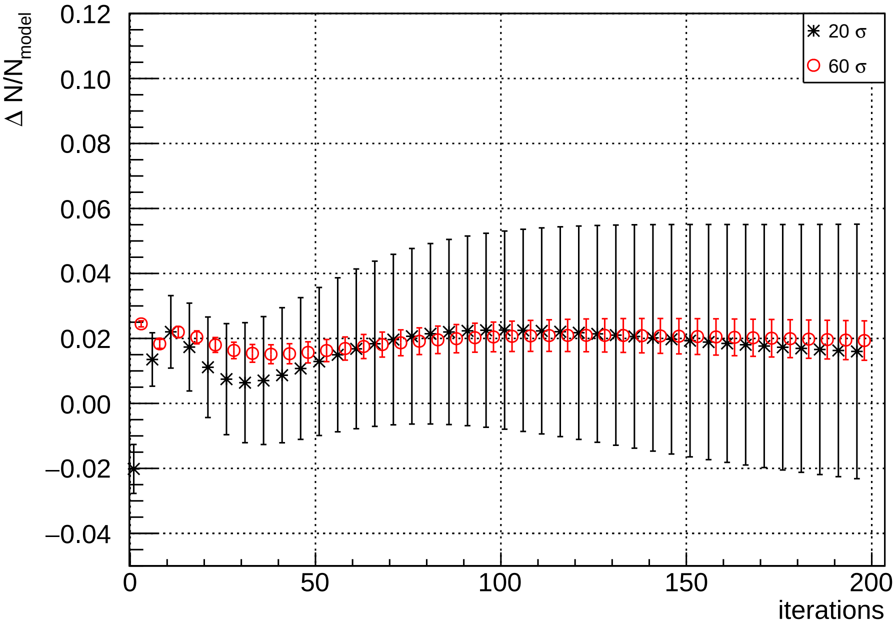

Figure 6.12: The deviation of the event number during the deconvolution compared to the number of events of the undeconvoluted *excess*-map as a function of the number of iterations. The deviation means the difference between the number of events of the deconvoluted *excess*-map to the number of events to the undeconvoluted *excess*-map normalised to the events of the undeconvoluted *excess*-map. The error is the standard error of 20 simulations.

7 Deconvolution of Extended Sources

So far the deconvolution of point sources was discussed. In the wavelength range of gamma rays, typical point sources are blazars which are a subcategory of active galactic nuclei [31]. In contrast to blazars, supernova remnants have an extended morphology [32]. Deconvolution algorithms are extremely useful to study the morphology of extended sources. By means of deconvolution, the angular resolution of an astronomical image can be improved. Unlike for a point source, not the 68%-radius is the indication of the improvement of the match between the simulated image and the source model during the deconvolution, but the relative error. The relative error has a minimum. For further iterations, the resolution of the image deteriorates again. Hence, the iteration number of the minimum of the relative error represents an optimum of the iterations which provides the best resolution of the data.

In this chapter the deconvolution of extended sources with a ring-shaped and a Gaussian morphology as an example for extended sources is discussed. In order to understand the influence of the deconvolution on the data, the dependence of the optimal iteration number on the significance, the lifetime and the size of the sources was studied. Thus, it is possible to chose the optimal iteration number to achieve the maximal resolution for the gamma-ray image of a source. The knowledge of the optimal iteration number of a source is therefore crucial for the deconvolution of real data.

The simulation of a Gaussian morphology and a ring structure were presented in Chapter 5.2 and 5.3. All deconvolutions were performed with the RCL. The results for both source morphologies are presented parallel to allow a comparison.

7.1 Study of the Influence of the Significance

The strong influence of the significance on the behaviour of the relative error in the case of a point source was already presented in Chapter 6.2. The focus is now on the impact of the significance on the relative error of a deconvoluted gamma-ray image of an extended source. In Figure 7.1, the relative error as a function of the number of iterations for ring-shaped sources with different significances is shown. The size of the underlying ring structure of the source is defined by the inner radius r_{in}=0.1 deg and the outer radius r_{out}=0.3 deg. The error is the standard error of 20 simulations.

The relative error increases with decreasing significance. Furthermore, the standard error for smaller significances is larger than for higher significances and grows with the number of iterations. The same behaviour was already observed for the relative error in the case of a point source and was discussed in Chapter 6.2. Another striking feature in Figure 7.1 is that the minimum of the relative error RE_{min} depends on the significance. For higher significances,

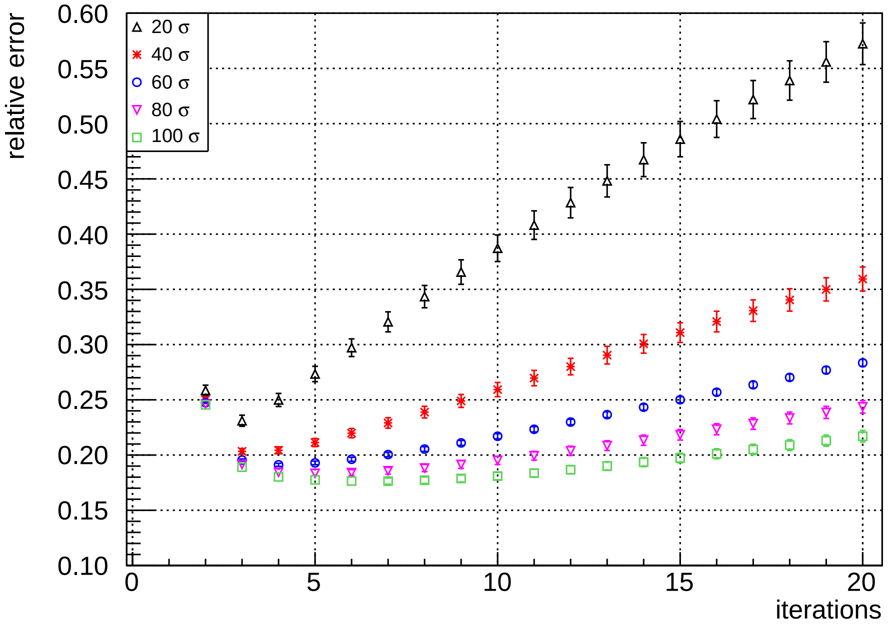

Figure 7.1: The dependence of the relative error as function of the number of iterations for a ring-shaped source with different significances. The size of the underlying ring structure of the source model is defined by the the inner radius $r_{\rm in}$=0.1 deg and the outer radius $r_{\rm out}$=0.3 deg. The error is the standard error of 20 simulations.

$RE_{\rm min}$ is located at higher iteration numbers. The iteration number at which $RE_{\rm min}$ is positioned, represents hence the optimal iteration number. More iterations are not reasonable since the relative error would grow again and thus, the match between the deconvoluted image and the source model would deteriorate again.

To study the influence of the significance on $RE_{\rm min}$ in more detail, the optimal iteration number as a function of the significance of a ring-shaped source is presented in Figure 7.2. The size of the underlying ring structure of the source model is $r_{\rm in}$=0.1 deg and $r_{\rm out}$=0.3 deg. The error is the standard error of 20 simulations. One can clearly see that the optimal iteration number increases for higher significances of the source. Simultaneously the standard error grows with the significance. In comparison to the results of the deconvolution of a ring-shaped source, the optimal iteration number as a function of the significance of a Gaussian-shaped source is shown in Figure 7.3. The size of the Gaussian model is defined by the 68%-radius of the Gaussian $d_{\rm Gauss}$=0.1 deg. The error is the standard error of 20 simulations. As for the ring-shaped source, the optimal iteration number increases with the significance.

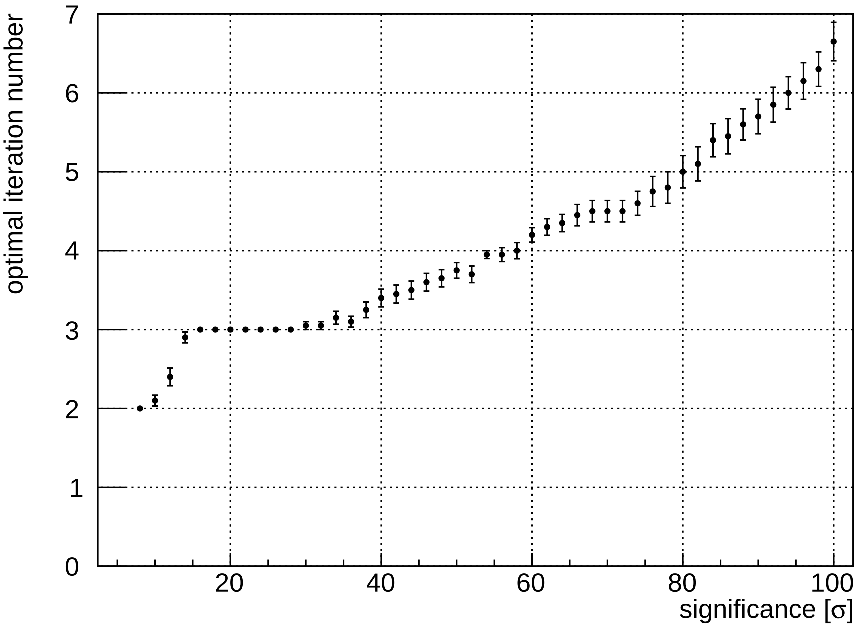

Figure 7.2: The optimal iteration number as a function of the significance of a ring-shaped source with r_{in} =0.1 deg and r_{out} =0.3 deg. The error is the standard error of 20 simulations.

To explain the observed dependence of the optimal iteration number on the significance of the source, one has to keep in mind in which way sources with different significances differ from each other. The brighter a source, the better the source morphology stands out of the background. It is therefore not surprising that the deconvoluted image of a bright source matches more with the original model than the deconvoluted image of a weak source. In the case of a weak source more statistical fluctuations are interpreted as signal and are intensified with every further iteration step. Thus, also the optimal iteration number is smaller, which is demonstrated in Figure 7.2 and Figure 7.3. Since extended sources with a more complicated morphology than point sources are regarded, the contrast of the source morphology to the background is crucial for the deconvolution. Due to the fact that sources with higher significances include more source events, the extended source morphology is better pronounced than compared to a weaker source with less events. Consequently, the difference of the relative error between higher and lower significances can be seen even more clearly than it was the case for the point source in Chapter 6.2.

Another notable feature in Figure 7.2 and Figure 7.3 is the standard error, which is zero for some significances. In this case, all simulations resulted in the same optimal iteration number. Within the zones in which the standard error is zero, the optimal iteration number is for several significances constant and forms a plateau. These plateaus are smaller and less pronounced for higher significances or do not occur any more. AS a result one can choose quite surely the optimal iteration number for the deconvolution of gamma-ray sources with

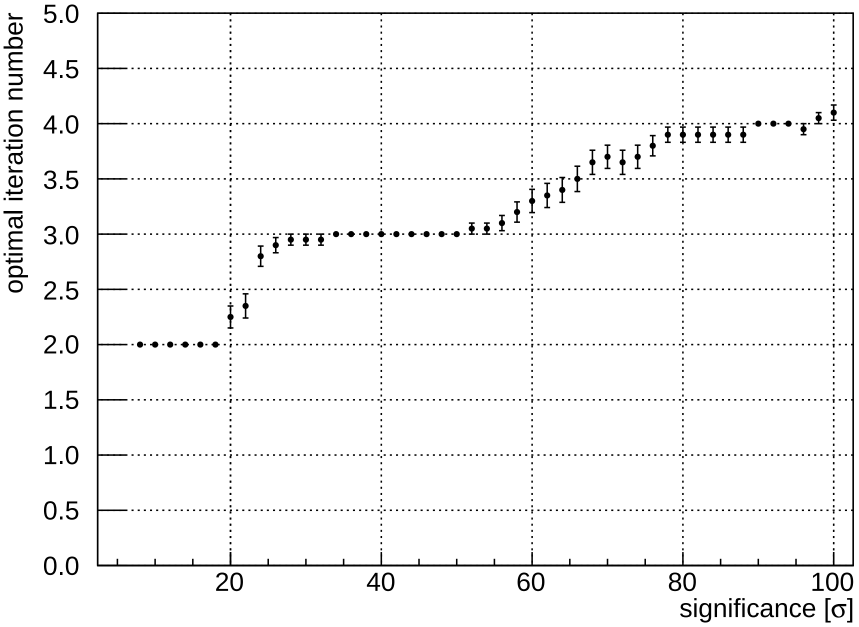

Figure 7.3: The optimal iteration number as a function of the significance of a Gaussian-shaped source with d_{Gauss}=0.1 deg. The error is the standard error of 20 simulations.

significances inside theses plateaus. Outside of the plateau the choice is less clear and one has to weight between two possible optimal iteration numbers in consideration of the standard error.

7.2 Study of the Influence of the Lifetime

The number of OFF-events in the simulation is calculated from the lifetime as was explained in Chapter 6.1. It can be adjusted by scaling the number of events of the analysis of the supernova remnant RX J1713.7-3946 [23] for which the lifetime is known. Since the number of ON-events depends directly on the number of OFF-events within the source region and therefore on the lifetime, one expects that the lifetime as well as the significance both influence the relative error and hence, also the optimal iteration number.
In Figure 7.4, the optimal iteration number as a function of the lifetime for a ring-shaped source is shown. The size of the underlying ring structure of the source model is r_{in}=0.1 deg and r_{out}=0.3 deg. The error is the standard error of 20 simulations. For comparison, the optimal iteration number as a function of the lifetime for a Gaussian-shaped source is shown in Figure 7.5. The size of the underlying Gaussian model is d_{Gauss}=0.1 deg. The error is the standard error of 20 simulations.

For the ring-shaped source the optimal iteration number increases with growing lifetime. In contrast, the influence of the lifetime on the optimal iteration number of a Gaussian-shaped source is small. The optimal iteration decreases slowly with a slope of -0.0008±0.0004 with growing lifetime (cf. Figure 7.5). Therefore, the difference of the results for the optimal iteration number for different life times in the case of a Gaussian-shaped source is negligible.

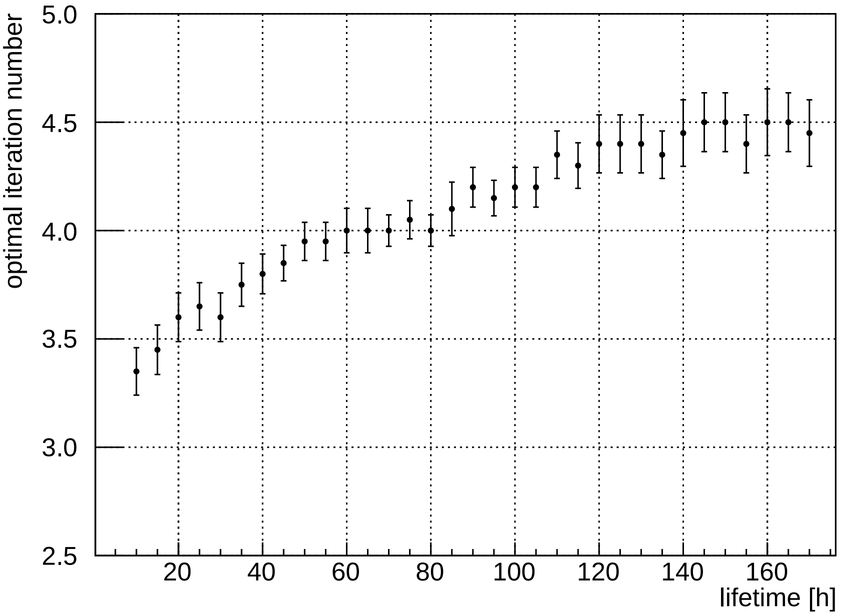

Figure 7.4: The optimal iteration number as a function of the lifetime of a ring-shaped source with r_{in} =0.1 deg and r_{out}=0.3 deg. The significance of the source is 60 σ. The error is the standard error of 20 simulations.

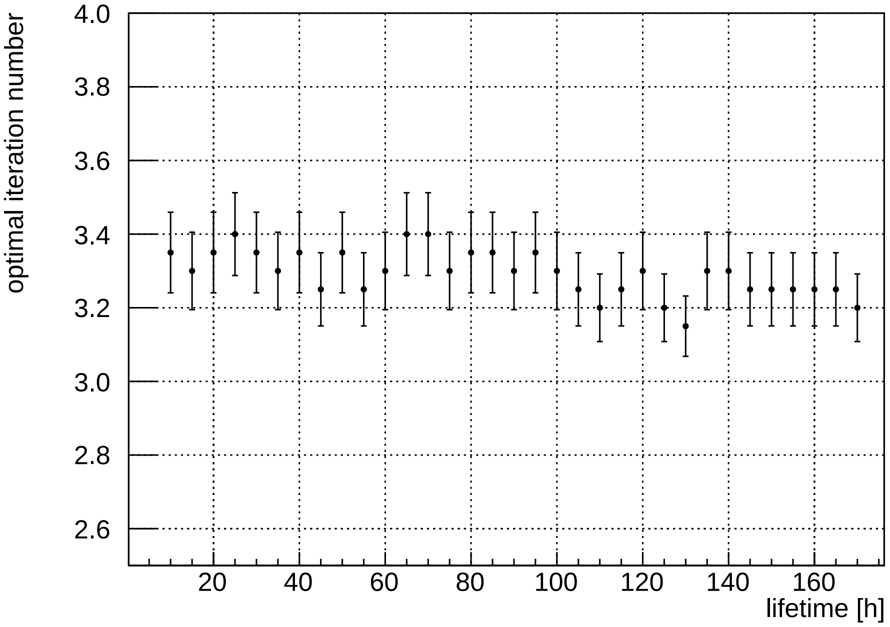

Figure 7.5: The optimal iteration number as a function of the lifetime for an Gaussian-shaped source with d_{Gauss}=0.1 deg The significance of the source is 60 σ. The error is the standard error of 20 simulations.

To understand the difference between the result for the two extended sources, one has to study the morphology of their models: in the case of a ring-shaped source, the ring model is a ring-shaped plateau with steep sides. On the other hand, the slope of a Gaussian model is much more extended due to the slow decrease of the Gaussian. For a Gaussian with d_{Gauss}=0.1 deg the 99%-radius of the model is 0.28 deg and thus, much larger as d_{Gauss}. As a consequence the area of a Gaussian-shaped source with d_{Gauss}=0.1 deg is nearly of the same size as the area of a ring structure with r_{in}=0.1 deg and r_{out}=0.3 deg.

Furthermore, there is a certain difference in the calculation of the OFF-events of a Gaussian-shaped source and a ring-shaped source: the OFF-events of the Gaussian-shaped source are calculated within its 99%-radius, the OFF-events of the ring-shaped source are calculated within the fourfold radius of r_{out}, which corresponds to a circle with a radius of 1.2 deg around the source centre. The number of OFF-events of a ring-shaped source is hence much larger than the number of OFF-events of a comparable Gaussian-shaped source. As a result also the number of ON-events for a the ring-shaped source is much larger than for a Gaussian-shaped source. The ratio of the number of ON-events to the area of the source for both morphologies is listed in Table 7.1. The area of the source is in the case of Gaussian source the area within the 99%-radius and for a ring-shaped source the area within r_{in} and r_{out}. If one regards the ratio of the number of ON-events to the source area for different lifetimes, the result is notable: in the case of a ring-shaped source the ratio of the ON-events to the area increases significantly more than for a Gaussian-shaped source. Hence, an increasing lifetime leads to much

more additional ON-events in the simulation of a ring-shaped source and thus, to a better pronounced morphology than it is the case of the simulation of a Gaussian-shaped source.
Besides the different development of the ratio of the number of ON-events to the area in dependence of the lifetime, the shape of the morphology is of particular interest. As already stated above, the morphology of the ring structure model is a ring-shaped plateau with steep sides. The ON-events are uniformly distributed over the source area. For the Gaussian-shaped model it is the contrary: due to the probability distribution of the Gaussian the ON-events are mainly distributed in the centre of the source model. However, there exists a small probability for the ON-events to be distributed far away of the centre. This probability leads to statistical fluctuations, which can be interpreted as signal and intensified by the deconvolution algorithm. Because of these false interpreted fluctuations additional ON-events provided by a higher lifetime can also lead to a smaller optimal iteration number. Due to the probability-distribution of the morphology of a Gaussian-shaped it is likely to occur more often than for a ring-shaped source.

In summary, the difference of the behaviour of the optimal iteration number in dependence on the lifetime between a Gaussian source and a ring-shaped source is caused by the different numbers of OFF-events of both morphologies. Furthermore, a growing lifetime leads to a smaller increase of ON-events in the case of a Gaussian source compared to a ring-shaped source. In addition the extended morphology of a Gaussian results in higher probability of misinterpretation of fluctuations as signal during the deconvolution.
To take the better results for higher lifetimes at least for the ring-shaped source into account, in all simulations of extended sources a lifetime of 100 h was used, if not otherwise stated.

morphology	lifetime [h]	$N_{\mathrm{ON}}/A_{\mathrm{source}}$ [1/deg^2]
ring	100	36704
ring	170	55017
Gaussian	100	18908
Gaussian	170	21651

Table 7.1: Ratio of ON-events to the area of the simulation of the gamma-ray image of a ring-shaped source with r_{in}=0.1 deg and r_{out}=0.3 deg and a Gaussian-shaped source with d_{Gauss}=0.1 deg. The significance of the sources is 60 σ each.

7.3 Study of the Influence of the Morphology

A deconvolution shall improve the angular resolution of a gamma-ray image to enable a deeper investigation of the morphology of a source. However, the morphology has a strong impact on the deconvolution itself and hence on the optimal iteration number.
In order to study the influence of the width and the radius of a ring-shaped source separately, the width of the ring, defined as $d_{\mathrm{ring}} = r_{\mathrm{out}} - r_{\mathrm{in}}$, and radius of the ring, defined as $R = r_{\mathrm{in}} + d_{\mathrm{ring}}/2$, are hereby introduced. The size of a Gaussian-shaped source is indicated by d_{Gauss}. In this section the influence of the size parameters on the optimal iteration number is discussed.

In Figure 7.6 the optimal iteration number as a function of the radius R for a ring-shaped source with different d_{ring} is shown. The significance of the source is $60\,\sigma$. The error is the standard error of 20 simulations. One can clearly see that the optimal iteration number decreases with increasing R. Moreover, the optimal iteration number is for some radii of the source constant and forms a plateau. Inside these zones it is straightforward to chose the optimal iteration number for the application of the deconvolution algorithm on real data of a source similar to the simulated one. Outside of these plateaus the iteration number fluctuates more and the choice of the optimal iteration number is more difficult.
Also a strong dependence of the optimal iteration number on d_{ring} is striking. The optimal

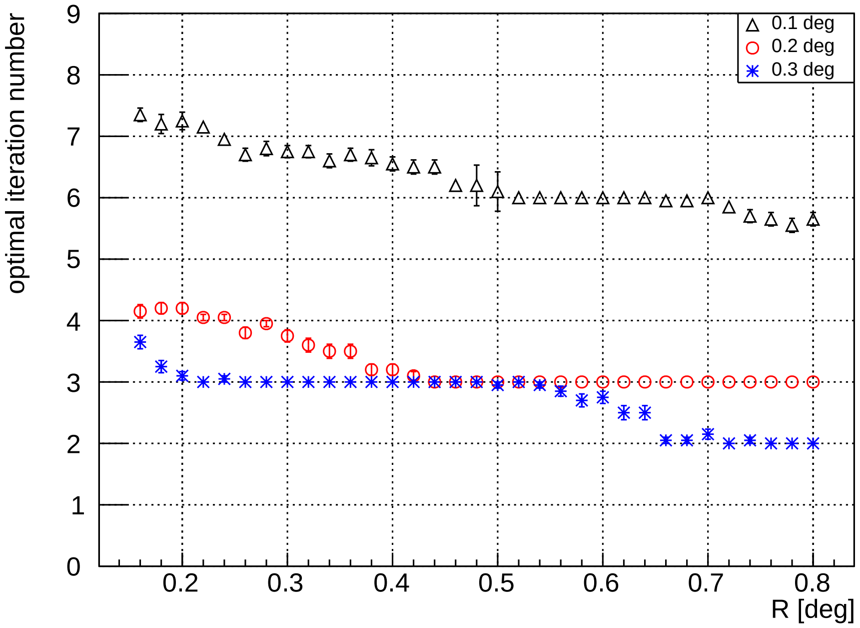

Figure 7.6: The optimal iteration number as a function of the radius R for a ring-shaped source with different d_{ring} of 0.1 deg, 0.2 deg and 0.3 deg. The significance of the source is $60\,\sigma$. The error is the standard error of 20 simulations.

iteration number for a narrow ring with d_{ring}=0.1 deg is significantly higher than for broader ring structures. Furthermore, the results of d_{ring}=0.1 deg and d_{ring}=0.2 deg are much more different to each other than the results of d_{ring}=0.2 deg and d_{ring}=0.3 deg in comparison.
To study the influence of d_{ring} on the optimal iteration number in more detail, in Figure 7.7 the optimal iteration number as a function of d_{ring} for a ring-shaped source with R=0.3 deg is plotted. The significance of the source is 60 σ. The error is the standard error of 20 simulations.

Striking is here as well that a smaller d_{ring} leads to a higher optimal iteration number than a larger d_{ring}. This can be explained by the increasing source area A_{ring} of the ring for larger d_{ring}, which is listed for different d_{ring} in Table 7.2. In comparison the area $A_{4\mathrm{r}_{\mathrm{out}}}$, which is defined by the fourfold radius r_{out} around the source centre, increases less with d_{ring}. Within

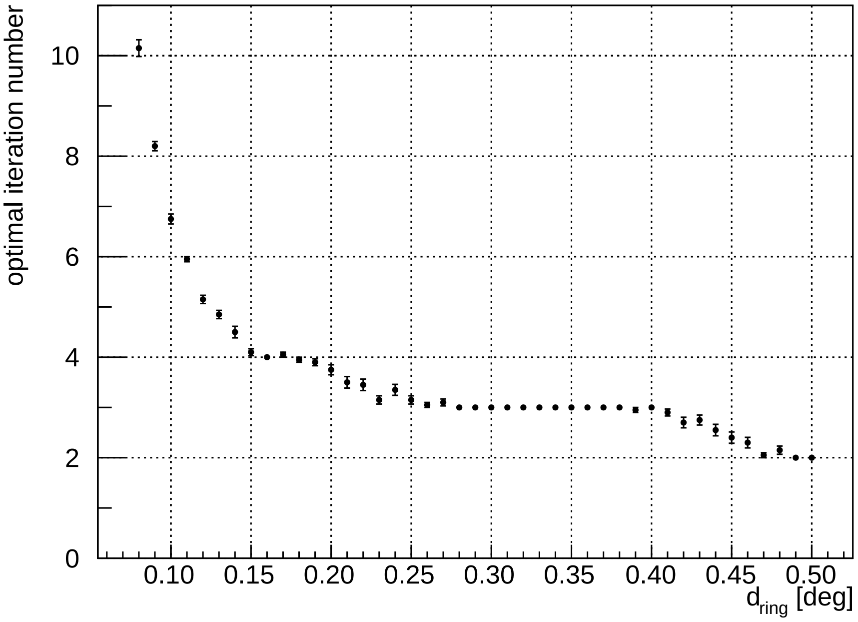

Figure 7.7: The optimal iteration number as a function of d_{ring} for a ring-shaped source with R=0.3 deg. The significance of the source is 60 σ. The error is the standard error of 20 simulations.

R [deg]	d_{ring} [deg]	A_{ring} [deg^2]	$A_{4\mathrm{r}_{\mathrm{out}}}$ [deg^2]
0.3	0.1	0.57	10.18
0.3	0.2	0.38	8.04
0.3	0.3	0.19	6.16

Table 7.2: Source area A_{ring} and $A_{4\mathrm{r}_{\mathrm{out}}}$ of the simulation of the gamma-ray image of ring-shaped source for different d_{ring} and fixed R. A_{ring} is the area between r_{in} and r_{out}, in which the ON-events are distributed. $A_{4\mathrm{r}_{\mathrm{out}}}$ is defined by the fourfold radius r_{out} around the source centre in order to calculated the number of OFF-events.

R [deg]	d_{ring} [deg]	$N_{\mathrm{ON}}/A_{\mathrm{ring}}$ [1/deg^2]	$N_{\mathrm{OFF}}/A_{4\mathrm{r_{out}}}$ [1/deg^2]
0.3	0.1	65100	4319
0.3	0.2	35481	4066
0.3	0.3	24469	3479

Table 7.3: Ratio of ON-events to the source area and ratio of OFF-events to $A_{4\mathrm{r_{out}}}$ for the simulation of the gamma-ray image of ring-shaped source for different d_{ring} and fixed R.

$A_{4\mathrm{r_{out}}}$, the number of OFF-events is calculated. Due to the number of ON-events in turn depends on the number of OFF-events, the number of ON-events increases with increasing $A_{4\mathrm{r_{out}}}$. Though, the area $A_{4\mathrm{r_{out}}}$ and hence, the number of ON-events grows slower than the source area A_{ring}, in which the ON-events are distributed. Thus, the ratio of ON-events per source area $N_{\mathrm{ON}}/A_{\mathrm{ring}}$ is significant smaller for larger d_{ring} than for smaller d_{ring} as can be seen in Table 7.3. Consequently it is in line with the expectations that d_{ring} has a strong influence on the behaviour of the optimal iteration number.

Moreover, the optimal iteration number does not depend linearly on d_{ring}, which can also be seen in Figure 7.6. The same is apparent if one regards $N_{\mathrm{ON}}/A_{\mathrm{ring}}$ for different d_{ring} (cf. Table 7.3). Even more striking is this feature for the ratio of OFF-events to the area $A_{4\mathrm{r_{out}}}$: the ratio $N_{\mathrm{OFF}}/A_{4\mathrm{r_{out}}}$ depends on d_{ring} and hence on r_{out}. To understand this, one has to take into account that the OFF-events are calculated within a large circle around the source centre of the acceptance map. The acceptance map drops to the edges. Thus, it is comprehensible that a narrow ring-shaped source with a small r_{out} and a small d_{ring} has more OFF-events and hence, ON-events per area than a more extended ring-shaped source due to the influence of the acceptance. Consequently the morphology of a narrower source is more pronounced which leads to higher optimal iteration number.

In Figure 7.8 the optimal iteration number as a function of d_{Gauss} for a Gaussian-shaped source is shown. The significance of the source is $60\,\sigma$. The error is the standard error of 20 simulations. As well as for the ring structure, also the optimal iteration number for the Gaussian-shaped source decreases with increasing size of the source. Furthermore, one can see that the optimal iteration number drops apparently faster with growing size than in the case of the ring-shaped source. However, one has to keep in mind, that the actual size of the Gaussian-shaped source is much larger than d_{Gauss} as was already explained in Chapter 7.2. Therefore, the result in Figure 7.8 are in line with the expectations.

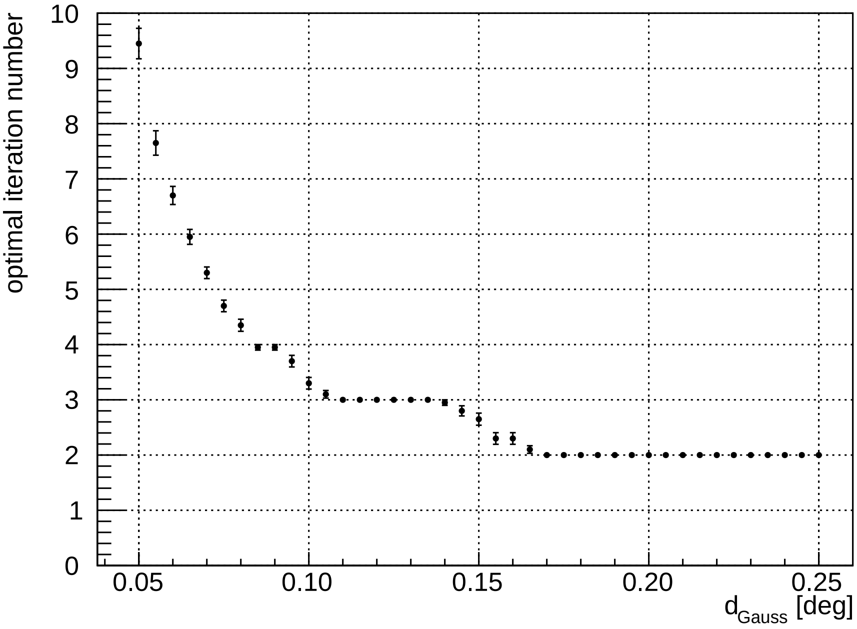

Figure 7.8: The optimal iteration number as a function of d_{Gauss} for a Gaussian-shaped source. The significance of the source is $60\,\sigma$. The error is the standard error of 20 simulations.

8 Supernova Remnant RX J1713.7-3946

In the previous chapter the simulation of gamma-ray sources and their deconvolution was discussed. The used PSF and camera acceptance were taken from the already mentioned analysis of the supernova remnant RX J1713.7-3946 [23]. RX J1713.7-3946, which is also known as G347.3-05, is the brightest and best studied young supernova remnant in the range of VHE gamma-rays. It was the first gamma-ray source to be resolved spatially and enabled comprehensive studies of morphology and spatially resolved spectra. Furthermore, it allows insights into the acceleration process of charged particles within a supernova remnant, which is described theoretically by the model of diffusive shock acceleration [33, 34]. RX J1713.7-3946 is therefore one of the most important sources of VHE gamma-rays.

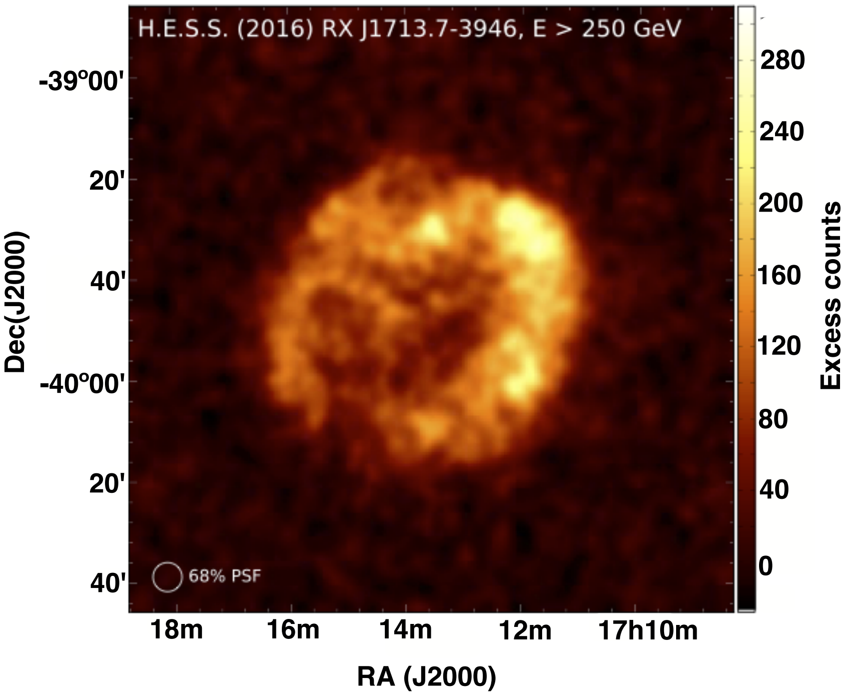

Figure 8.1: Excess count image of RX J1713.7-3946, which was corrected by the reconstruction acceptance. The image was smoothed with a two-dimensional Gaussian of width 0.03 deg. The size of the PSF is demonstrated by the white circle in the bottom left corner.

The supernova remnant RX J1713.7-3946 is located in the constellation Scorpius in the galatic plane and is a strong gamma-ray as well as X-ray source with a shell-type morphology. It was first discovered in the year 1996 in the soft X-ray waveband by ROSAT. In the VHE regime RX J1713.7-3946 was observed in two distinct observation campaigns by H.E.S.S. The first one was in the years 2003-2005, the second one took place in 2011 and 2012. In Figure 8.1, the excess count image of RX J1713.7-3946 is shown. The image was smoothed with a two-dimensional Gaussian of width 0.03 deg. The size of the PSF is indicated by the white circle in the bottom left corner. [33, 34, 35].

Despite the previous morphological studies of the supernova remnant, the origin of the VHE gamma-ray emission of RX J1713.7-3946 is so far unclear. There are two possible scenarios for the generation of gamma-rays: in a leptonic scenario, gamma-rays are produced due to synchrotron losses of accelerated particles in the shock front via the inverse Compton effect of relativistic electrons with ambient low energy photons (cf. Chapter 2.3.2). In the hadronic scenario gamma-rays are emitted via the generation and decay of neutral pions (cf. Chapter 2.3.1). However, there are some indications which contradict to a pure leptonic or hadronic scenario. In the case of a leptonic scenario the presence of a weak magnetic field is required to reduce the energy loss of the electrons [36]. That disagrees to the model of diffusive shock acceleration, which does not include any kind of magnetic field amplification in the shock. On the other hand, in the scenario of hadronic origin a high gas density is required. In this case one would expect to observe also strong thermal X-ray emission. Such X-ray emission was not detected for RX J1713.7-3946 [36]. Due to these uncertainties of the production of gamma-rays in RX J1713.7-3946, whether leptonic, hadronic or a mixture of both, further investigations are required [33].

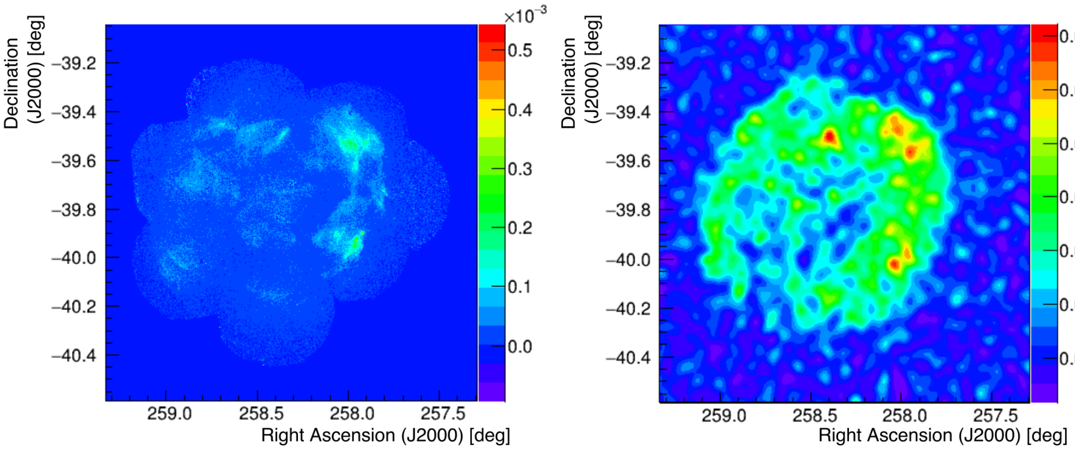

(a) (b)

Figure 8.2: (a) X-ray image of RX J1713.7-3946, detected by XMM-Newton. (b) Gamma-ray image of RX J1713.7-3946, deconvoluted with RCL after six iterations. [33]

It is, for example, assumed, that magnetic field amplification in the vicinity of clumps due to shock-clump interactions increases the synchrotron X-ray emission, which would support the hadronic scenario. To study the origin of the gamma-ray emission, it is therefore promising to study the morphology of RX J1713.7-3946. One way is thereby to compare the VHE gamma-ray image of the supernova remnant to its X-ray image, observed by XMM-Newton in the energy range of 1 keV to 10 keV [33].

In order to compare the X-ray image to the gamma-ray image, the Pearson's correlation coefficient is calculated between both data sets. Beforehead, the gamma-ray image was deconvoluted by the RCL to improve its resolution. In Eq. 8.1 [36] the Pearson's correlation coefficient $r_{X-ray,VHE}$ is defined:

$$r_{X-ray,VHE} = \frac{\sum_i (z_{i,X-ray} - \bar{z}_{X-ray})(z_{i,VHE} - \bar{z}_{VHE})}{\sqrt{(z_{i,X-ray} - \bar{z}_{X-ray})^2}\sqrt{(z_{i,VHE} - \bar{z}_{VHE})^2}} \tag{8.1}$$

The sum is the sum over all bins i in the image. The bin content of a bin i is denoted in the case of the X-ray image as $z_{i,X-ray}$, whereas for the gamma-ray image as $z_{i,VHE}$. $\bar{z}_{X-ray}$ and $\bar{z}_{VHE}$, respectively, are the mean values of the bin content of all bins in the image.

As one can see in Figure 8.2 (b), the morphology of RX J1713.7-3946 deviates from a perfect ring structure. Thus, to determine the optimal iteration number, a modified ring model of RX J1713.7-3946 is required, which reflects the individual morphology of the supernova remnant. In this thesis the result of Sebastian Heinz for the optimal iteration number was used [22].

The deconvolution of the gamma-ray image of RX J1713.7-3946 was performed with six iterations. Thereby an angular resolution of 0.024 deg can be reached considering a point source.

In Figure 8.2, the X-ray image and the deconvoluted gamma-ray image after six iterations of RX J1713.7-3946 are shown.

The correlation between the X-ray image and the gamma-ray image was calculated within an annular region defined by a radius of 0.2 deg to 0.6 deg in respect to the centre of the remnant. The radii are chosen in order to make sure that the X-ray source as well as the gamma-ray source are included. In Figure 8.3, the Pearson's correlation coefficient in dependence of the bin size for the deconvoluted and undeconvoluted gamma-ray image is shown.

The Pearsons's correlation coefficient for the deconvoluted case is nearly constant for a bin size smaller than 0.04 deg. In this range the correlation coefficient varies only slightly from 0.69 to 0.72. For bin sizes larger than 0.04 deg the coefficient fluctuates more. Apart from that, the results show that X-ray data correlates well with the gamma-ray data. In comparison to the deconvoluted case, the unconvoluted gamma-ray image correlates far less to the X-ray data. Only from a bin size of more than 0.04 deg, the correlation coefficients of both the convoluted as well as the convoluted case are at the same scale. This coincidences with the fact, that the 68%-radius of the PSF (and hence, the angular resolution of the undeconvoluted image) is 0.048 deg. Therefore, a higher correlation of the undeconvoluted image is not to expect for smaller bin sizes [36].

For a more detailed investigation of the correlation between X-rays and gamma-rays in the supernova remnant, the image was separated in five sub-regions, which are shown in Figure

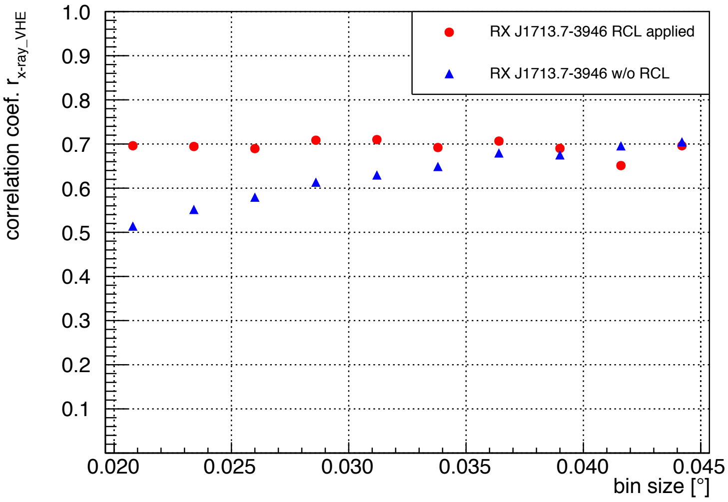

Figure 8.3: Pearson's correlation coefficient as a function of the bin size for the deconvoluted and non deconvoluted gamma-ray image of RX J1713.7-3946.

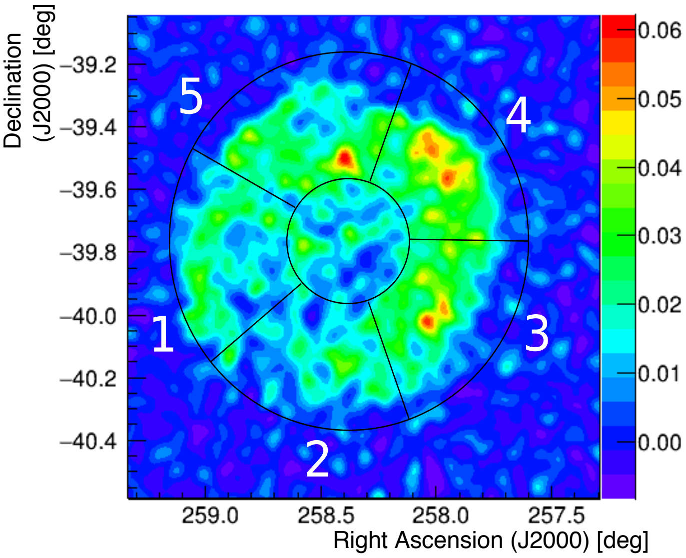

Figure 8.4: H.E.S.S. gamma-ray image separated in five sub-regions between a radius of 0.2 deg to 0.6 deg, in order to compare gamma-ray data and X-ray data [33]. The angular borders of all regions are listed in Table 8.1. The Pearson's correlation coefficient was calculated for every region.

	whole shell	1	2	3	4	5
starting angle ϕ_1	0 deg	240 deg	160 deg	90 deg	20 deg	310 deg
stopping angle ϕ_2	360 deg	310 deg	240 deg	160 deg	90 deg	20 deg
$r_{X-ray,VHE}$	0.70	0.45	0.56	0.68	0.80	0.67

Table 8.1: Radial coordinates of the sub-regions in the gamma-ray image for the correlation study of RX J1713.7-3946 and Pearson's correlation coefficient for five selected sub-regions [33].

8.4. The sub regions are defined with the radial coordinates of the above-named annular region, i.e. the radii 0.2 deg and 0.6 deg and the angles ϕ_1 and and ϕ_2. The radii are fixed for all subregions, the angles are listed in Table 8.1 and were also used in the H.E.S.S. analysis of RX J1713.7-3946 [33]. The Pearson's correlation coefficient was calculated for a bin size of 0.021 deg. The results are also listed in Table 8.1.
The region with the highest correlation coefficient is region 4 with a value of 0.80. Region 3 and region 5 have almost the same correlation coefficient of 0.68 and 0.67, respectively. In these three regions a high gamma-ray emission was observed and also the X-ray-emission is higher than for the other regions. Region 1 has the lowest correlation coefficient of 0.45.

As a result of the correlation study, it can be concluded that the X-ray data and the VHE gamma-ray data of the supernova remnant RX J1713.7-3946 are well correlated. In contrast, two distinct correlation studies with different deconvolution algorithms led to the result that VHE gamma rays and the proton distribution of the ISM are only weakly correlated [36, 37]. In a hadronic scenario one would expect that the gamma-ray emission due to neutral pion decay is correlated to the proton distribution of the ISM. Hence, the combined results of the correlation studies support a leptonic scenario via the inverse Compton scattering between high-energetic photons and the ambient photon field. This result challenges the hadronic model which have so far been used to explain the observed spectra [38]. Furthermore, the result of the correlation study is consistent to observations of RX J1713.7-3946 by Fermi LAT. These support a leptonic origin as well [39].

9 Summary and Outlook

In this thesis the influence of deconvolution algorithms on simulated gamma-ray images with different source morphologies was investigated.

As deconvolution algorithm mainly the Richardson-Lucy algorithm was used. In order to compare the results of the RCL to another algorithm, the Maximum-Entropy algorithm was utilised as well. The influence of the deconvolution was studied in dependence of the morphology of a point source and of extended sources. As examples of extended sources a Gaussian-shaped source and a ring-shaped source were examined.

In the case of a point source the behaviour of the 68%-radius, i.e. the angular resolution, during the deconvolution was discussed. Different source properties and their influence on the results of the deconvolution as the significance, the lifetime and the binning were studied. Furthermore, the behaviour of the relative error which is a measure of the deviation of the deconvoluted image to the original source model was studied, dependent on the number of iterations. It was concluded that the deconvolution of brighter sources lead to a better angular resolution. A bright source with a significance of 100σ reached an 68%-radius of 0.013 deg after 200 iteration whereas a source with a significance of 20σ reached a 68%-radius of 0.016 deg. In both cases the deconvolution resulted in a significant improvement compared to the 68%-radius of the undeconvoluted image with 0.048 deg. The influence of the lifetime is negligible in contrast to the significance. The difference of the 68%-radius of sources with a significance of 60σ and lifetimes of 25 h and 100 h, respectively, after 140 iterations is less than 0.0005 deg. A rebinning of 5 of the gamma-ray image has proven to be good to provide a sufficient resolution and to avoid long run times.
The relative error decreases continuously with increasing number of deconvolutions. The number of events is conserved during the convolution as required for the application of a deconvolution algorithm.

Besides the point source, the behaviour of the relative error during the deconvolution of extended sources was studied. The relative error has a minimum after few iterations. This minimum represents the optimal iteration number which provides the best match of the simulated image and the source model. The optimal iteration number increases with growing significance for the Gaussian-shaped source and the ring-shaped source. If more iterations are possible, a better match with the original model can be reached. Hence, brighter sources can be deconvoluted better. The influence of the lifetime is negligible small in the case of the Gaussian-shaped source. The optimal iteration number of Gaussian-shaped source with a significance of 60σ and d_{Gauss}=0.1 deg is around 3.3 and decreases slowly with a slope of -0.0008±0.0004. In contrast, for the ring-shaped source of the same significance a larger lifetime results in a higher optimal iteration number. A ring-shaped source with a size defined by r_{in} =0.1 deg and r_{out}=0.3 deg and a lifetime of 10 h has a optimal iteration number of 3.35, whereas the same ring-shaped source with a lifetime of 170 h has a optimal iteration number of 4.45. For both morphologies the size of the source has a strong influence on the results of the deconvolution. An increasing source area leads to a smaller optimal iteration number. Thus, less improvement is achieved via deconvolution for larger sources compared to smaller ones.

As an application of the deconvolution, the gamma-ray image of the supernova remnant RX J1713.7-3946 was deconvoluted. Afterwards, a correlation study of RX J1713.7-3946 was performed. In this study the Pearson's correlation coefficient between the X-ray image and gamma-ray image of RX J1713.7-3946 was calculated. The calculation was made for different bin sizes of the deconvoluted gamma-ray image as well as for the undeconvoluted gamma-ray image. The calculation for the deconvoluted image resulted in a higher correlation factor for bin sizes smaller than the 68%-radius of the PSF. For a bin size of 0.021 deg for example, the correlation factor of the deconvoluted image was 1.35 times higher compared to the undeconvoluted one. In this way, it was shown that the application of deconvolution allows to prove correlation between X-ray data and gamma-ray data for smaller structures. This result underpins the leptonic scenario of the origin of gamma radiation via the process of inverse Compton scattering.

The application example of the correlation study supports the idea that deconvolution algorithms are a powerful tool to gain more insight into the acceleration processes within the supernova remnant RX J1713.7-3946 as well as other galactic sources. Further work needs to be done to understand the influence of deconvolution on the data in more detail. For this the binning of the gamma-ray image and the influence of the lifetime have to be examined more deeply. Moreover, resulting studies of the optimal iteration number in the case of extended source morphologies can serve as look-up tables.
Furthermore, it is recommended to study the deconvolution of real sources by means of modified models different from the ideal source morphologies which were presented in this thesis. These models could reflect the individual morphology of a real source in contrast to a idealised morphology. The investigation of such simulations can be used to improve the application of deconvolution algorithms on real sources, for example to choose the optimal iteration number. In addition, an important issue is the comparison of different deconvolution algorithms. Thus, it can be demonstrated whether different deconvolution algorithms, even if they behave quite differently, lead to the same result. This is fundamental, because it means that deconvolution algorithms provide real results. The results of such comparison studies could help to choose the appropriate algorithm for a given task. The future application of deconvolution algorithms could thereby be performed more effective.

In conclusion it can be said that deconvolution algorithms are useful to enhance our understanding of the origin of VHE gamma-rays. Therefore, the application of deconvolution algorithm shall be encouraged in prospective research.

Bibliography

[1] W. Hofmann. *Astrophysics with H.E.S.S.* 2012 (accessed December 3, 2018). URL: https://www.mpi-hd.mpg.de/hfm/HESS/pages/about/physics/.

[2] V.F. Hess. "Über Beobachtungen der durchdringenden Strahlung bei sieben Freiballonfahrten". In: *Physikalische Zeitschrift 13* (1912), pp. 1084–1091.

[3] J.J. Beatty J.J. Beatty and S.P. Wakely. "Cosmic Rays". In: (Oct. 2017). URL: http://pdg.lbl.gov/2018/reviews/rpp2018-rev-cosmic-rays.pdf.

[4] H.E.S.S. Collaboration, Fabio Acero and H. Gast. 2011 (accessed December 3, 2018). URL: https://www.mpi-hd.mpg.de/hfm/HESS/hgps/figures/hess_hgps_montage.jpg.

[5] L. Woltjer. "Supernova Remnants". In: 10 (1972), p. 129. DOI: 10.1146/annurev.aa.10.090172.001021.

[6] T. Padmanabhan. *Theoretical Astrophysics*. Vol. 2. Cambridge University Press, 2001. DOI: 10.1017/CBO9780511840159.

[7] D. Bhattacharya. "On the morphology of supernova remnants with pulsars". In: *Journal of Astrophysics and Astronomy* 11.2 (June 1990), pp. 125–140. ISSN: 0973-7758. DOI: 10.1007/BF02715012. URL: https://doi.org/10.1007/BF02715012.

[8] ENRICO Fermi. "On the Origin of the Cosmic Radiation". In: *Phys. Rev.* 75 (8 Apr. 1949), pp. 1169–1174. DOI: 10.1103/PhysRev.75.1169. URL: https://link.aps.org/doi/10.1103/PhysRev.75.1169.

[9] M.S. Longair. *High Energy Astrophysics*. English. Cambridge University Press, 2011. ISBN: 9781139494540.

[10] C. Grupen et al. *Astroparticle Physics*. Springer, 2005. ISBN: 9783540253129.

[11] Yung-Su Tsai. "Pair production and bremsstrahlung of charged leptons". In: *Rev. Mod. Phys.* 46 (4 Oct. 1974), pp. 815–851. DOI: 10.1103/RevModPhys.46.815. URL: https://link.aps.org/doi/10.1103/RevModPhys.46.815.

[12] J. Matthews. "A Heitler model of extensive air showers". In: *Astropart. Phys.* 22 (2005), pp. 387–397. DOI: 10.1016/j.astropartphys.2004.09.003.

[13] W. Heitler. *Quantum theory of radiation*. 1954.

[14] Hermann Kolanoski. *Einführung in die Astroteilchenphysik*. 2009.

[15] Boris Shwartz Claus Grupen. *Particle Detectors*. Cambrigde CB2 8BS, United Kingdom: Cambrigde University Press, 2008.

[16] Mark Thompson. *Modern particle physics*. Cambrigde CB2 8BS, United Kingdom: Cambrigde University Press, 2013.

[17] F. A. Aharonian et al. “Measurement of the radial distribution of Cherenkov light generated by TeV gamma-ray air showers”. In: *Astropart. Phys.* 10 (1999), pp. 21–29. DOI: 10.1016/S0927-6505(98)00039-5. arXiv: astro-ph/9807119 [astro-ph].

[18] H.E.S.S. collaboration. *H.E.S.S. High Energy Stereoscopic System*. 2018 (accessed December 3, 2018). URL: https://www.mpi-hd.mpg.de/hfm/HESS/.

[19] Trevor C. Weekes. “The Atmospheric Cerenkov imaging technique for very high energy gamma-ray astronomy”. In: *International WE - Heraeus Summer School: Physics with Cosmic Accelerators Bad Honnef, Germany, July 5-16, 2004*. 2005. arXiv: astro-ph/0508253 [astro-ph].

[20] W. Benbow. “The H.E.S.S standard analysis technique”. In: *Prepared for 7th Workshop on Towards a Network of Atmospheric Cherenkov Detectors* (2005). DOI: https://www.mpi-hd.mpg.de/hfm/HESS/pages/publications/proceedings/Conf_Palaiseau_2005/Benbow.pdf.

[21] Konrad Bernlohr. “Simulation of Imaging Atmospheric Cherenkov Telescopes with CORSIKA and sim$_t$*elarray*”. In: *Astropart. Phys.* 30 (2008), pp. 149–158. DOI: 10.1016/j.astropartphys.2008.07.009. arXiv: 0808.2253 [astro-ph].

[22] Sebastian Heinz. “A Detailed Study of the Supernova Remnant RCW 86 in TeV γ-Rays”. PhD thesis. Friedrich-Alexander-Universität Erlangen-Nürnberg, 2012. URL: https://ecap.nat.fau.de/wp-content/uploads/2017/05/2012%5C_Heinz%5C_Dissertation.pdf.

[23] David Berge, S. Funk, and J. Hinton. “Background Modelling in Very-High-Energy gamma-ray Astronomy”. In: *Astron. Astrophys.* 466 (2007), pp. 1219–1229. DOI: 10.1051/0004-6361:20066674. arXiv: astro-ph/0610959 [astro-ph].

[24] William Hadley Richardson. “Bayesian-Based Iterative Method of Image Restoration$*$”. In: *J. Opt. Soc. Am.* 62.1 (Jan. 1972), pp. 55–59. DOI: 10.1364/JOSA.62.000055. URL: http://www.osapublishing.org/abstract.cfm?URI=josa-62-1-55.

[25] David Stirzaker. *Elementary Probability*. 2nd ed. Cambridge University Press, 2003. DOI: 10.1017/CBO9780511755309.

[26] S. Heinz, I. Jung, and C. Stegmann. “Systematic studies of the Richardson–Lucy deconvolution algorithm applied to VHE gamma data”. In: *Astropart. Phys.* 36 (2012), pp. 146–150. DOI: 10.1016/j.astropartphys.2012.05.013.

[27] E.T. Jaynes and James H. Justice. “Bayesian Methods: General Background”. In: *Maximum Entropy and Bayesian Methods in Applied Statistics: Proceedings of the Fourth Maximum Entropy Workshop University of Calgary, 1984*. Cambridge University Press, 1986, pp. 1–25. DOI: 10.1017/CBO9780511569678.003.

[28] L. B. Lucy. “An iterative technique for the rectification of observed distributions”. In: *Astron. J.* 79 (1974), pp. 745–754. DOI: 10.1086/111605.

[29] John Skilling and Stephen F. Gull. “Bayesian maximum entropy image reconstruction”. English. In: *Spatial statistics and imaging*. Ed. by Antonio Possolo. Vol. Volume 20. Lecture Notes–Monograph Series. Hayward, CA: Institute of Mathematical Statistics, 1991, pp. 341–367. DOI: `10.1214/lnms/1215460511`. URL: `https://doi.org/10.1214/lnms/1215460511`.

[30] T.-P. Li and Y.-Q. Ma. “Analysis methods for results in gamma-ray astronomy”. In: 272 (Sept. 1983), pp. 317–324. DOI: `10.1086/161295`.

[31] C. M. Urry and P. Padovani. “Unified Schemes for Radio-Loud Active Galactic Nuclei”. In: 107 (Sept. 1995), p. 803. DOI: `10.1086/133630`. eprint: `astro-ph/9506063`.

[32] H. Abdalla et al. “The H.E.S.S. Galactic plane survey”. In: *Astron. Astrophys.* 612 (2018), A1. DOI: `10.1051/0004-6361/201732098`. arXiv: `1804.02432 [astro-ph.HE]`.

[33] H. Abdalla et al. “H.E.S.S. observations of RX J1713.73946 with improved angular and spectral resolution: Evidence for gamma-ray emission extending beyond the X-ray emitting shell”. In: *Astron. Astrophys.* 612 (2018), A6. DOI: `10.1051/0004-6361/201629790`. arXiv: `1609.08671 [astro-ph.HE]`.

[34] F. Aharonian et al. “A detailed spectral and morphological study of the gamma-ray supernova remnant rx j1713.7-3946 with h.e.s.s”. In: *Astron. Astrophys.* 449 (2006), pp. 223–242. DOI: `10.1051/0004-6361:20054279`. arXiv: `astro-ph/0511678 [astro-ph]`.

[35] Aharonian, F. et al. “Observations of the Crab nebula with HESS”. In: *A&A* 457.3 (2006), pp. 899–915. DOI: `10.1051/0004-6361:20065351`. URL: `https://doi.org/10.1051/0004-6361:20065351`.

[36] Sebastian Heinz Ira Jung-Richardt and Christian Stegman. “Detailed morphological studies of RX J 1713.7-3946 in very-high-energy gamma-rays”. In: (in preparation).

[37] Susanne Raab. private communication. 2018.

[38] Stefano Gabici and Felix A. Aharonian. “Hadronic gamma-rays from RX J1713.7-3946?” In: *Mon. Not. Roy. Astron. Soc.* 445 (2014), p. 70. DOI: `10.1093/mnrasl/slu132`. arXiv: `1406.2322 [astro-ph.HE]`.

[39] Fermi LAT Collaboration A. A. Abdo. “Observations of the Young Supernova Remnant RX J1713.7â3946 with the Fermi Large Area Telescope”. In: *The Astrophysical Journal* 734.1 (2011), p. 28. URL: `http://stacks.iop.org/0004-637X/734/i=1/a=28`.

Acknowledgments/Danksagung

Ich möchte mich bei folgenden Personen bedanken, die mich während meiner gesamten Arbeit unterstützt und begleitet haben. Mein besonderer Dank geht an:

- Herrn Prof. Dr. Stefan Funk für die Möglichkeit, meine Arbeit in dem faszinierenden Forschungsgebiet der Gammaastronomie schreiben zu dürfen.
- Frau PD Dr. Ira Richard-Jung für die hervorragende Betreuung und Unterstützung bei der Erstellung der Simulationen und Untersuchungen zu den Entfaltungsalgorithmen. Sie haben mir durch Ihre Erklärungen einem Zugang zu dem Verständnis von Simulationen und ihrer Entfaltung verschafft und mich durch vielfältige Ratschläge und Feedback im Verlauf meiner Arbeit sehr unterstützt. Danke, dass Sie immer ein offenes Ohr hatten.
- Susanne Raab, die mich insbesondere bei der Anwendung des Maximum-Entropie Algorithmus unterstützt und mir bei so mancher Frage rund um ROOT geholfen hat.
- Johannes Veh für die Hilfe bei allen Computerproblemen und das ausführliche Feedback beim Verbessern meiner Arbeit.
- Meine Büronachbarn, die schon bereits genannt wurden, nämlich Susanne und Johannes, für das angenehme Arbeitsumfeld und das gemeinsame Kochen.
- Stefan Eschbach für die Erklärungen zur Verwendung des Maximum-Entropie Algorithmus.
- Sebastian Heinz, den ich zwar nicht persönlich kennengelernt habe, aber dessen Programm zur Anwendung des Richardson-Lucy Algorithmus sehr hilfreich war.
- Allen in der Gammaastronomie-Arbeitsgruppe für die freundliche Atmosphäre und das häufige gemeinsame Kuchenessen und Grillen im Sommer.
- Allen, ob nun in der Abeitsgruppe oder in meinem Freundeskreis, die Teile meiner Arbeit gelesen und mir dazu Feedback gegeben haben.
- Gabriele Eckert, der Sekretärin des Lehrstuhls
- Meinen Freunden, die mich mit gemeinsamen Mittagessen und gelegentlichen Schafkopfpausen motiviert und ermutigt haben.
- Meiner Familie, für die Ermutigung und Unterstützung und insbesondere meiner Schwester für hilfreiche Englischkorrekturen.

Eigenständigkeitserklärung

Ich versichere hiermit, dass ich die vorliegende Masterarbeit mit dem Titel “Systematic studies of the deconvolution of gamma-ray images” selbstständig und ohne unzulässige fremde Hilfe erbracht habe. Ich habe keine anderen als die angegebenen Quellen und Hilfsmittel benutzt sowie wörtliche und sinngemäße Zitate kenntlich gemacht. Die Arbeit hat in gleicher oder ähnlicher Form noch keiner Prüfungsbehörde vorgelegen.

Ort, Datum

Unterschrift